Supplementary Information for

Unlocking electron transfer across carbon overlayers via single-atom engineered built-in electric field for industrial water purification

Tianran Sheng,[1,2,7] Xingen Lin,[1,6,7] Gang Zhao,[1,3] Ruoyan Wei,[1,5] Xiangyu Shu,[4] Cheng Qian,[1,2] Zhen Zhang,[4] Liangquan Sheng,[4]* Yude Su,[1,3]* Yafei Zhao[1,2]**

[1]State Key Laboratory of Precision and Intelligent Chemistry, School of Chemistry and Materials Science, University of Science and Technology of China, Hefei, Anhui 230026, China

[2]Deep Space Exploration Laboratory, University of Science and Technology of China, Hefei, Anhui 230026, China

[3]School of Nano Science and Technology, State Key Laboratory of Bioinspired Interfacial Materials Science, Suzhou Institute for Advanced Research, University of Science and Technology of China, Suzhou, Jiangsu 215123, China

[4]Biomass Oligosaccharides Engineering Technology Research Center of Anhui Province, Fuyang Normal University, Fuyang, Anhui 236037, China

[5]Institute of Biological Information Processing (IBI-3), Bioelectronics, Forschungszentrum Jülich, 52425 Jülich, Germany

[6]Southern Sichuan Gas District, PetroChina Southwest Oil & Gasfield Company, Luzhou, Sichuan 646001, China

[7]These authors contributed equally to this work.

*Correspondence to: yafeizhao@ustc.edu.cn; suyude@ustc.edu.cn; shenglq2015@163.com.

Experimental details

Chemicals. All chemicals used were of analytical grade and were employed without additional purification. Pluronic® P-123 (average M_n ~5,800) was acquired from Sigma-Aldrich. Melamine (99%) and TPP (triphenylphosphine) was sourced from Sinopharm Chemical Reagent Co., Ltd., China. TOP (trioctylphosphine, 95%) was purchased from LeYan, Shanghai Haohong Biological Pharmaceutical Technology Co., Ltd. PMS ($KHSO_5$·0.5$KHSO_4$•0.5K_2SO_4, ≥42% $KHSO_5$ basis), $Co(NO_3)_2$·$6H_2O$ (99.99%), phenyl ether (99%), 1,2-dichlorobenzene (99%, anhydrous), 1-octadecene (90%), FFA (98%), TBA (99%), *p*-BQ (99%), and TEMP (98%), PhOH (99.5%) and a series of substances to be degraded were obtained from Aladdin Bio-Chem Technology Co., China. MeOH (99.5%) and EtOH (99.7%) were sourced from General-reagent®, Shanghai Titan Scientific Co., Ltd. DMPO (99%) was purchased from Dojindo Laboratories Co., China. Other reagents not mentioned are obtained from Adamas, Titan. All aqueous solutions were prepared using purified water of Hangzhou Wahaha Group Co., Ltd.

Preparation of Co NP, Co_2P NP: The synthesis of Co NP followed standard procedures [1]. A N_2 fluxed flask was filled with TOPO (0.1 g, trioctylphosphine oxide). After adding 0.09 g (0.32 mmol) of oleic acid, which is used as a surfactant, dissolved in 12 mL of 1,2-dichlorobenzene, the solution was heated. When the temperature of the solution reached 170 °C, 0.52 g (1.52 mmol) of $Co_2(CO)_8$ dissolved in 4 mL of 1,2-dichlorobenzene was quickly injected. After the reaction progressed for 4 min, the heating mantle was removed and the reaction solution was cooled down in a water bath. The Co NPs were purified by adding ethanol and centrifuged (10000 rpm, 5 min, ＞20 °C). The supernatant was removed, and the NPs were redispersed in hexanes. The precipitation/redispersion process was performed twice overall. Finally, the obtained n-hexane solution was filtered through a PTFE membrane to remove large particles. To synthesize Co_2P NP, a flask which was filled with 12 mL of 1-octadecene and 3 mL TOP, was vacuumed at 100 °C for 30 min. Then the solution was fluxed with N_2 and heated up to 300 °C, the pre-synthesized Co NP (all) dispersed in the mixture of 3 mL 1-octadecene and 3 mL oleylamine (90% purity) were quickly injected into the solution and the reaction proceeded for 11 min. The solution was cooled to room

temperature by removal of the heating mantle. The NPs were separated by centrifugation and washed twice with ethanol/hexanes.

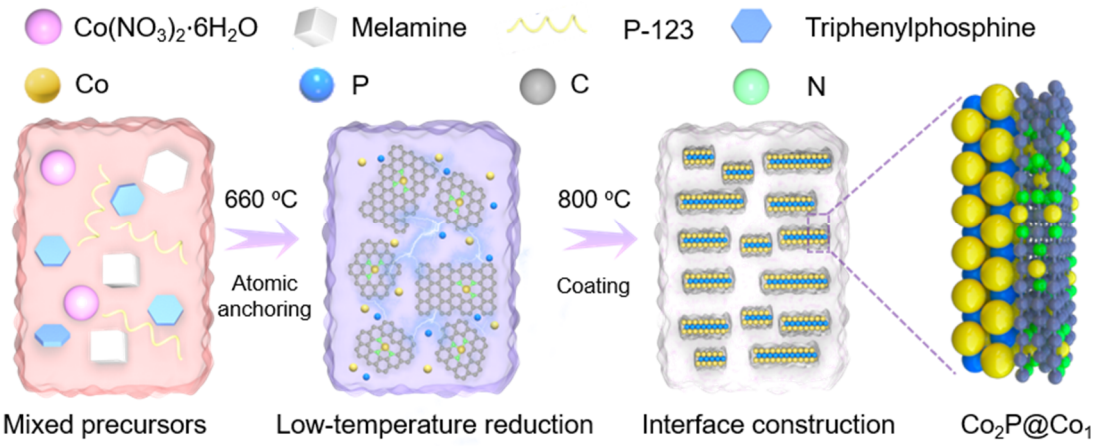
Preparation of Ni NP: In a typical experiment[2,3], $Ni(acac)_2$ (0.2 g, 0.78 mmol, nickel acetylactonate) was added to oleylamine (1.4 g) and 0.8 mL 1-octadecene. The mixture was degassed at 100 ºC and filled with N_2. Then, TOP (0.23 g, 0.8 equiv) was added and heated at 190 ºC for 1 h, giving quickly a black solution. The mixture was cooled to room temperature and centrifuged after addition of 4 mL of acetone to give a black product. The nanoparticles were redispersed in hexanes.

Preparation of Cu NP: In a typical experiment [4], $Cu(acac)_2$ (33 mg, 0.125 mmol, copper acetylactonate) was dissolved in 5 mL phenyl ether and 6 mL oleylamine. To this so-called royal blue solution 2 mmol of 1,2-tetradecanediol was added. The solution was stirred and degassed by three vacuum pump/backfill cycles under N_2. The temperature of the solution was slowly increased (~2 °C/min). When the color starts to turn yellow, maintain this temperature for 10 minutes (130–150 °C, and the temperature gradually increases as the amount of oleylamine increases.). Afterward, the solution was allowed to cool to room temperature, and the particles were precipitated from phenyl ether with ethanol and redispersed in toluene or hexane for further use. Noted that the temperature during the synthesis of nanoparticles was measured by a mercury thermometer inserted into the solution. All the obtained n-hexane solution was filtered through a 0.22 μm PTFE membrane to remove large particles.

Materials characterization. The organic compound concentration was determined by high-performance liquid chromatography (HPLC, Primaide, Hitachi Inc., Japan), equipped with a C18 (Shimadzu) column. The mobile phase was a mixture of water and methanol (V/V=40%:60%), with a flow rate of 1 mL/min. The leached metal ions were measured by ICP-AES (Optima 7300 DV, Perkin Elmer Inc., USA). The ROS were identified by EPR (JES-FA200, JEOL Co., Japan) under the following conditions: microwave power of 5.012 mW, sweep width of 100 G, modulation frequency of 100 kHz, modulation amplitude of 1.00 G, and 1000 points. The total organic carbon (TOC) concentration of the solutions was measured using a TOC analyzer (TOC-L CPHCN200, Shimadzu). ROS in the Co_2P@Co_1-PMS system using scavengers for $O_2{\cdot}^-$ scavengers such as *p*-BQ, for $^1O_2$ such as FFA, and for ·OH and $SO_4{\cdot}^-$ such as TBA,

and MeOH. ROS detection was conducted using spin-trapping EPR (ER200-SRC, Bruker Co., USA) at room temperature with DMPO and TEMP as spin-trapping agents. Specific experimental setups included: for the $^1O_2$ test, 1.0 mL of sample suspension was mixed with 40.0 μL of TEMP solution (50.0 $g \cdot L^{-1}$). For the detection of $\cdot OH$ and $SO_4\cdot^-$, 76.0 μL of sample suspension was combined with 4.0 μL of DMPO. The $O_2\cdot^-$ trapping-EPR assay was similarly conducted but a methanol medium was used. Reaction intermediates/products were analyzed by liquid chromatography coupled with an electrostatic field Orbitrap mass spectrometer (LC–Orbitrap MS) (Orbitrap XL ETD™, Thermo Fisher Scientific). Mass spectrometric detection was performed using electrospray ionization (ESI) in negative-ion mode, with the mass scan range set to m/z 50–500. Chromatographic separation was performed on a C18 column at a flow rate of 0.3 mL min^{-1}. A methanol/water mobile phase was used with gradient elution, in which the methanol fraction was increased from 15% to 95% according to the programmed LC method. The injection volume was 5 μL. For pathway interrogation, 10 mL of a 200/1000 ppm phenol solution was mixed with 1.25/1.5 mg $Co_2P@Co_1$ and 12/15 mg peroxymonosulfate (PMS). After reacting for 2 min, the suspension was filtered to remove solids. The filtrate was collected and stored at −20 °C prior to LC–MS analysis.

Supplementary Figures and Tables

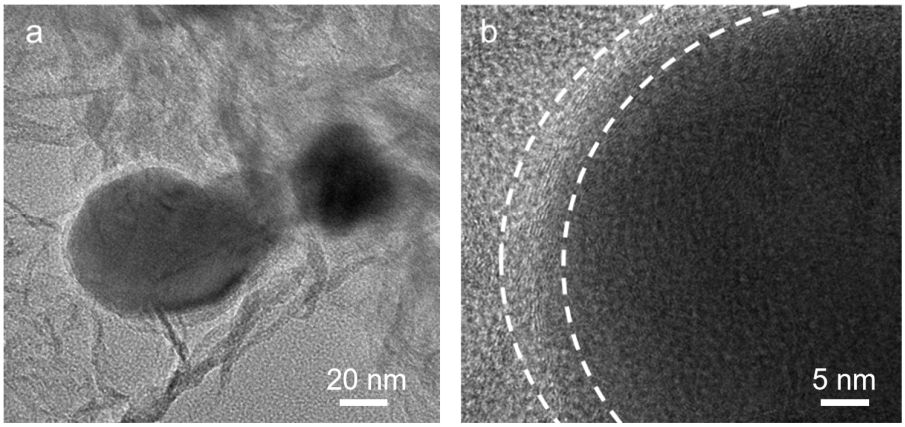


Supplementary Figure 1 | Two steps synthesis schematic.

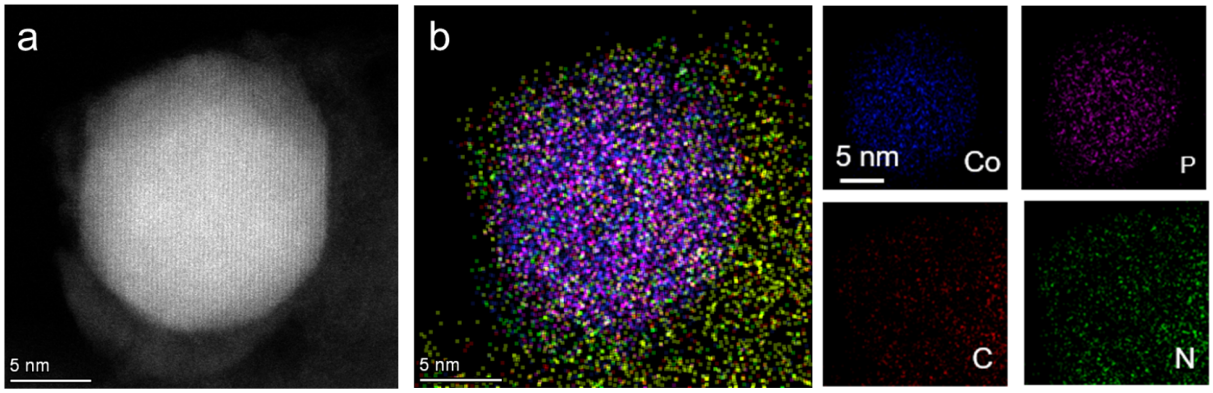


Supplementary Figure 2 | Synthesis device.

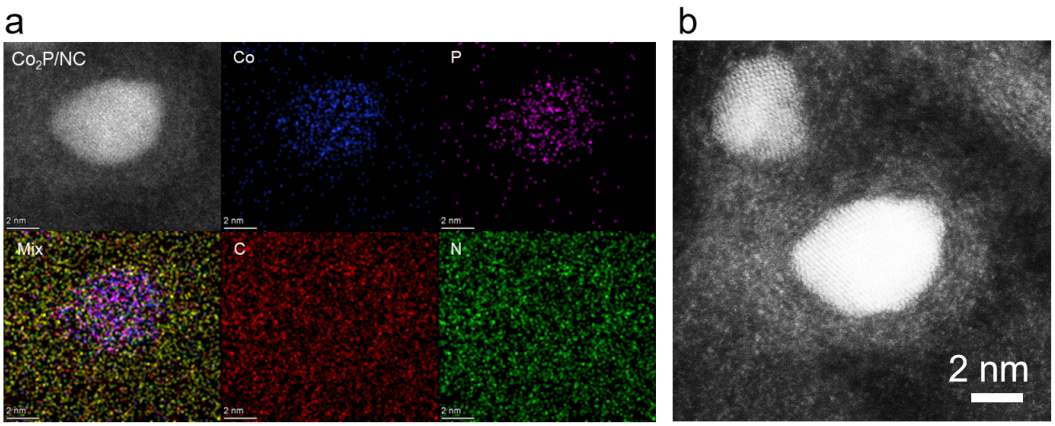
Note: The temperature required for the synthesis of nanoparticles was obtained from the thermometer in the figure.



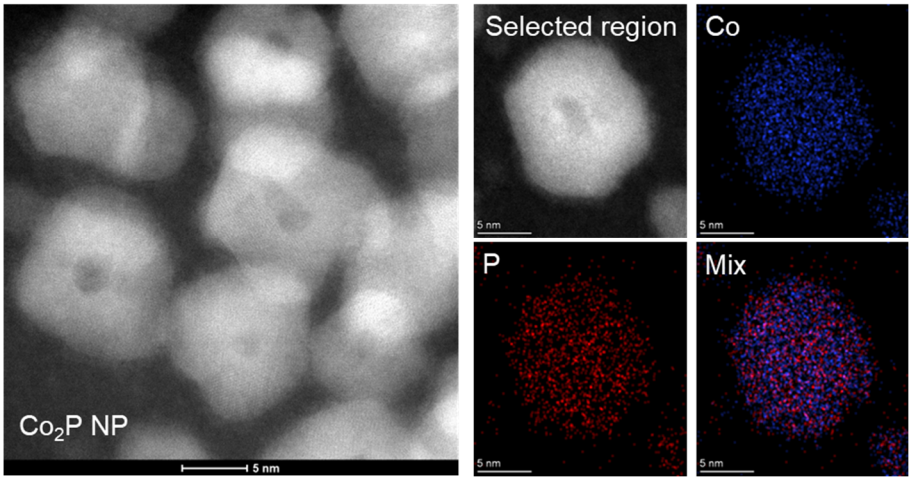
Supplementary Figure 3 | Bright-field TEM (BF-TEM) images of $Co_2P@Co_1$. (a) Low-magnification image showing particle morphology. (b) Enlarged view of an individual particle, revealing a core–shell structure, where the dashed lines indicate the boundary between the core and the surrounding shell layer.



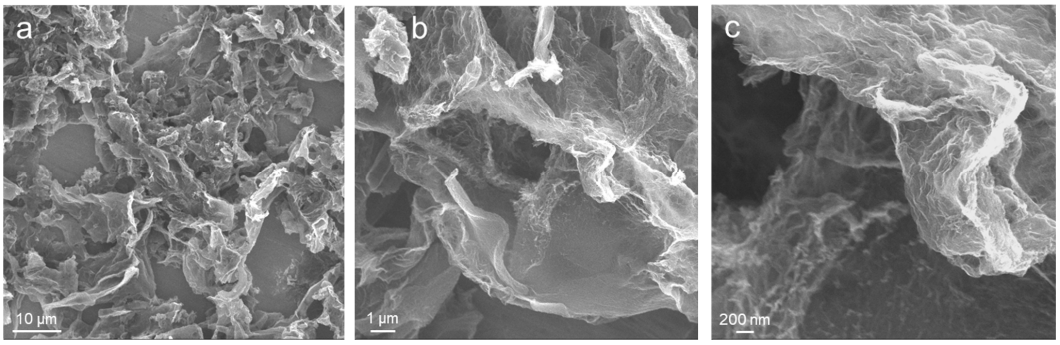
Supplementary Figure 4 | Elemental distribution of $Co_2P@Co_1$. TEM images (a) and corresponding EDS mappings of overlapped elements for $Co_2P@Co_1$.



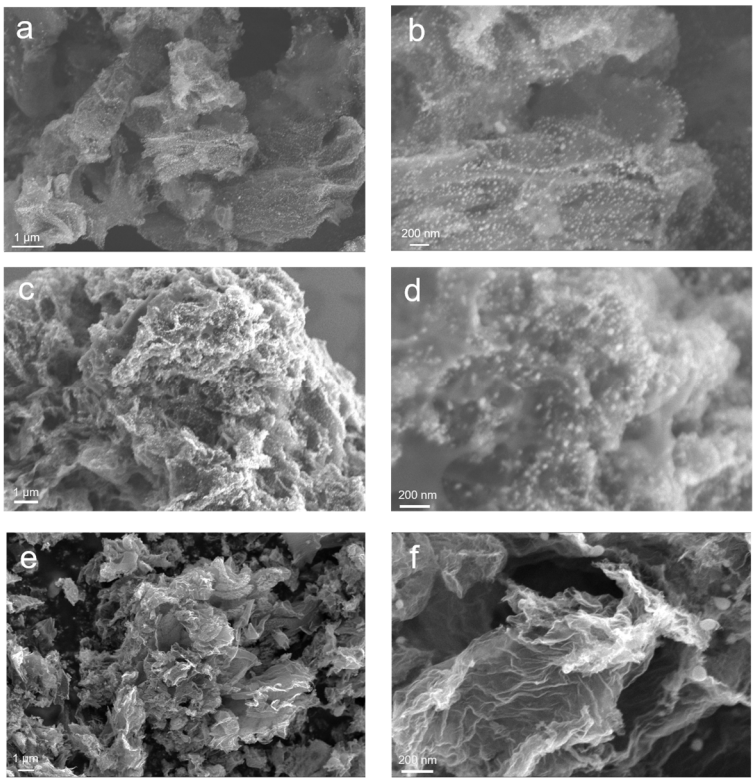
Supplementary Figure 5 | Elemental distribution of Co_2P/NC by EDS mapping.



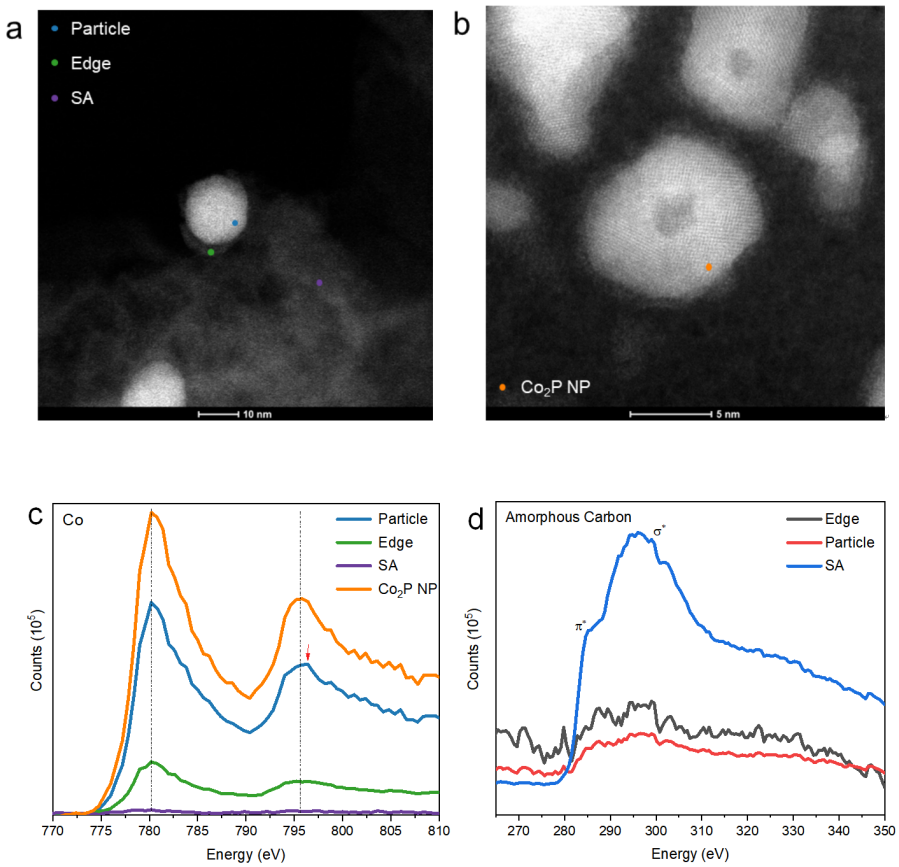
Supplementary Figure 6 | Elemental distribution of Co_2P NP by EDS mapping.



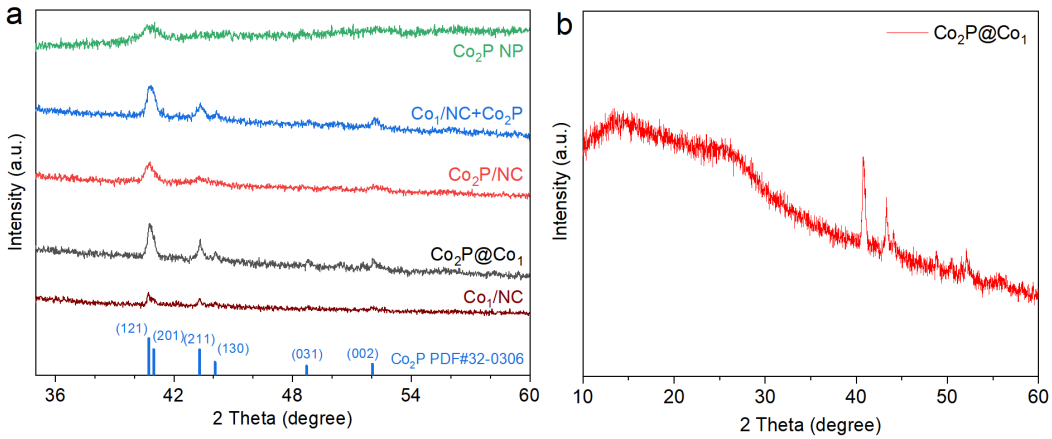
Supplementary Figure 7 | Scanning Electron Microscope (SEM) images. of NC with different magnification.



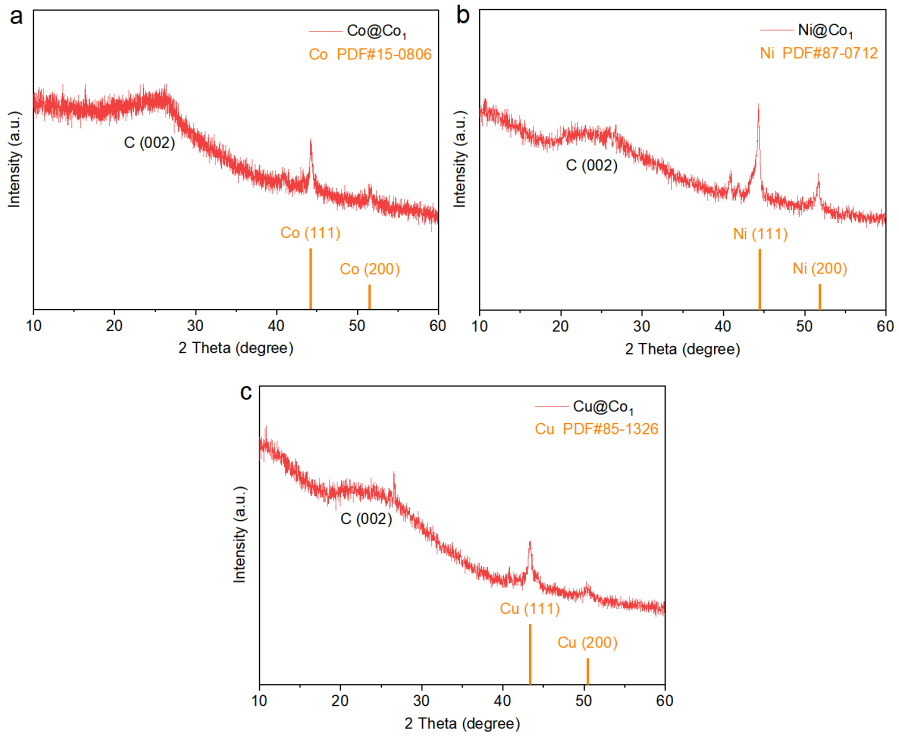
Supplementary Figure 8 | Scanning Electron Microscope (SEM) images. Co_1/NC+Co_2P (a, b), Co_2P/NC (c, d) and Co_1/NC (e, f).



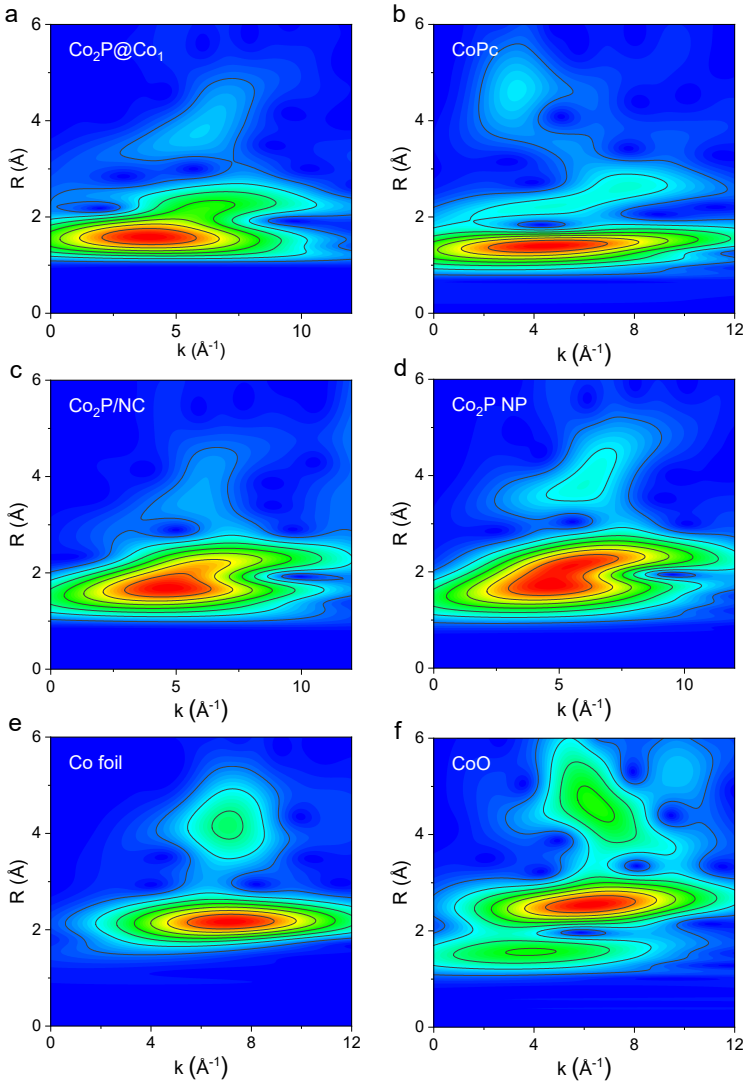
Supplementary Figure 9 | HAADF-STEM images of $Co_2P@Co_1$ (a) and Co_2P NP (b) with marked points for EELS analysis. Corresponding EELS spectra of Co L-edge (c) and C K-edge (d) acquired from the marked points in (a) and (b).



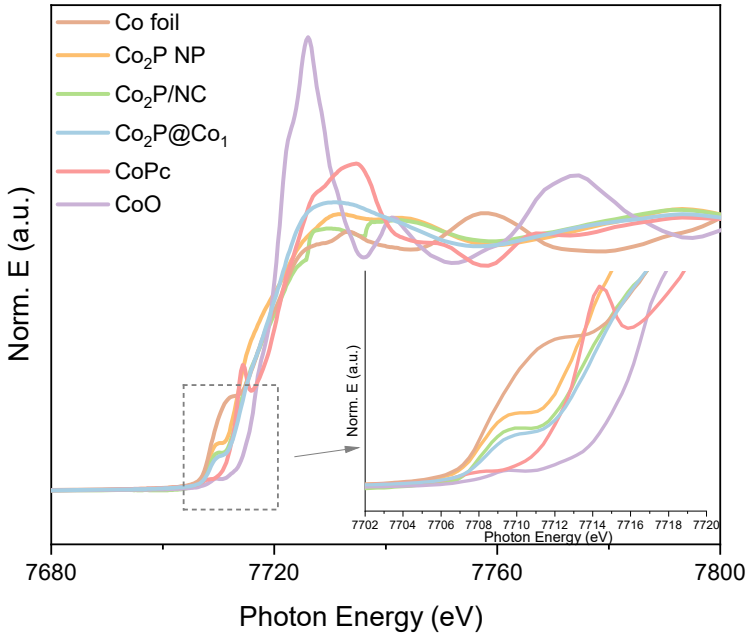
Supplementary Figure 10 | X-ray diffraction (XRD) patterns of different catalysts with Co (a) and larged angle range of $Co_2P@Co_1$ (b).



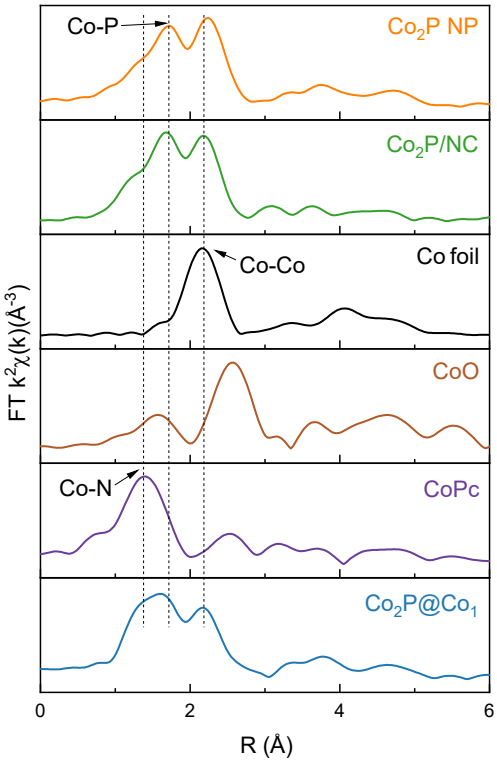
Supplementary Figure 11 | XRD patterns of Co@Co_1 (a), Ni@Co_1 (b), and Cu@Co_1 (c).



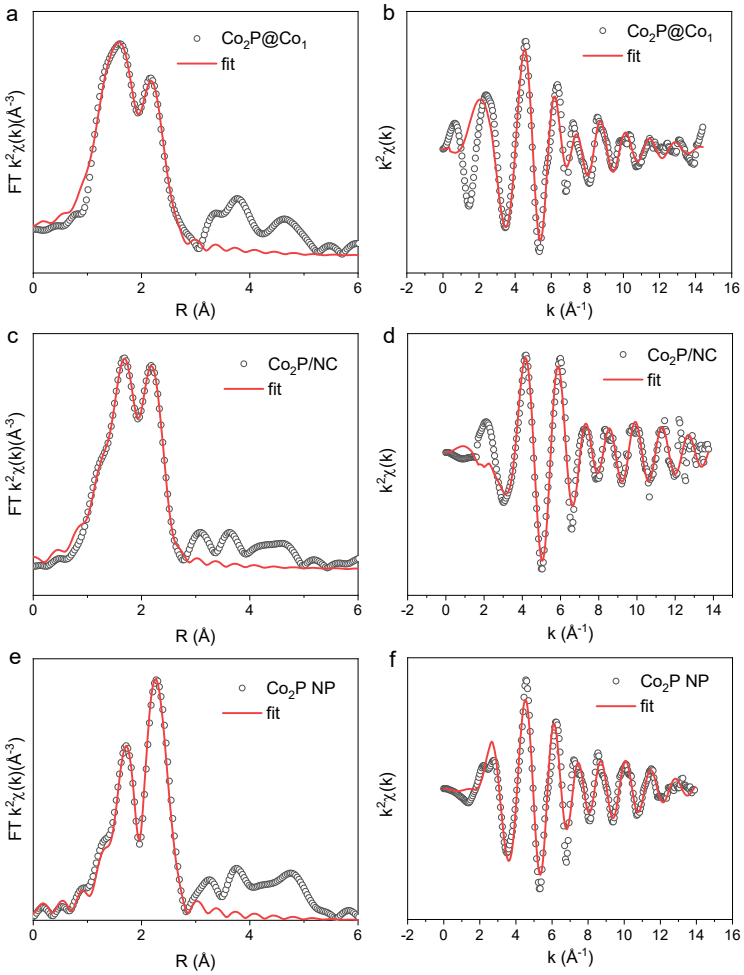
Supplementary Figure 12 | Wavelet transform of the EXAFS signal of $Co_2P@Co_1$ (a), CoPc (b), Co_2P/NC (c), Co_2P NP (d), Co foil (e) and CoO (f), showing the intensity distribution in k–R space.



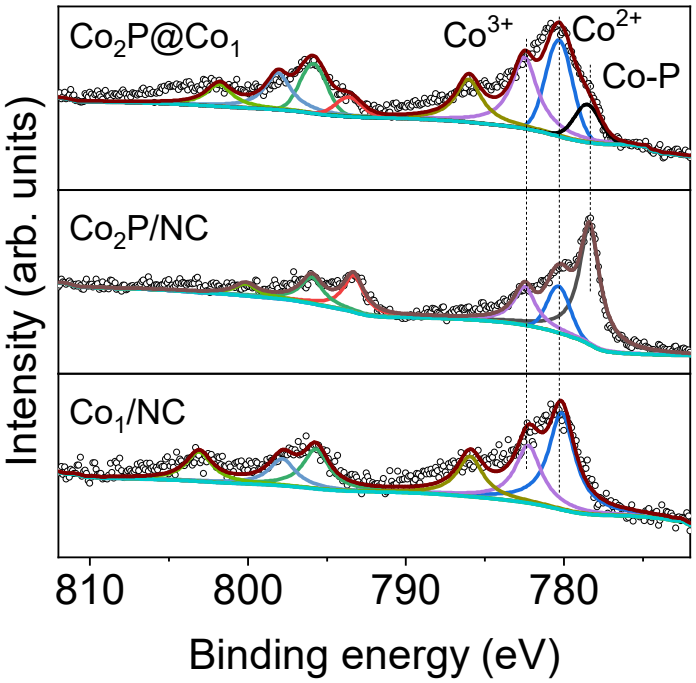
Supplementary Figure 13 | Co *K*-edge XANES spectra. The inset (right panel) shows an enlarged view of the absorption edge region (highlighted by the dashed box).



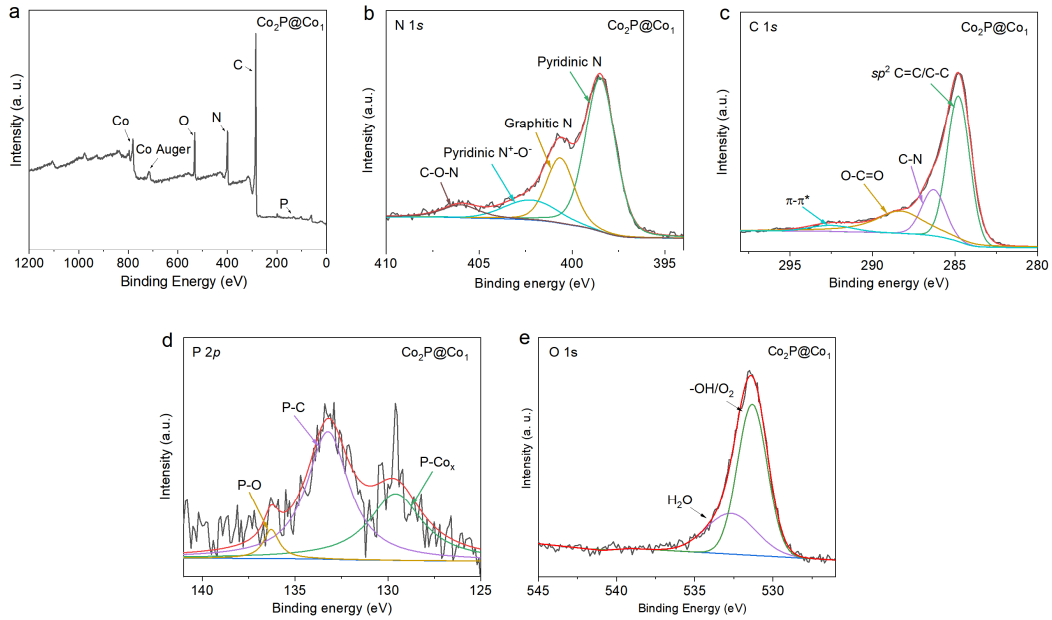
Supplementary Figure 14 | K^2-weighted EXAFS oscillations at the Co *K*-edge. The variations in oscillation features indicate differences in the local atomic structure, including coordination number and bond disorder around Co centers.



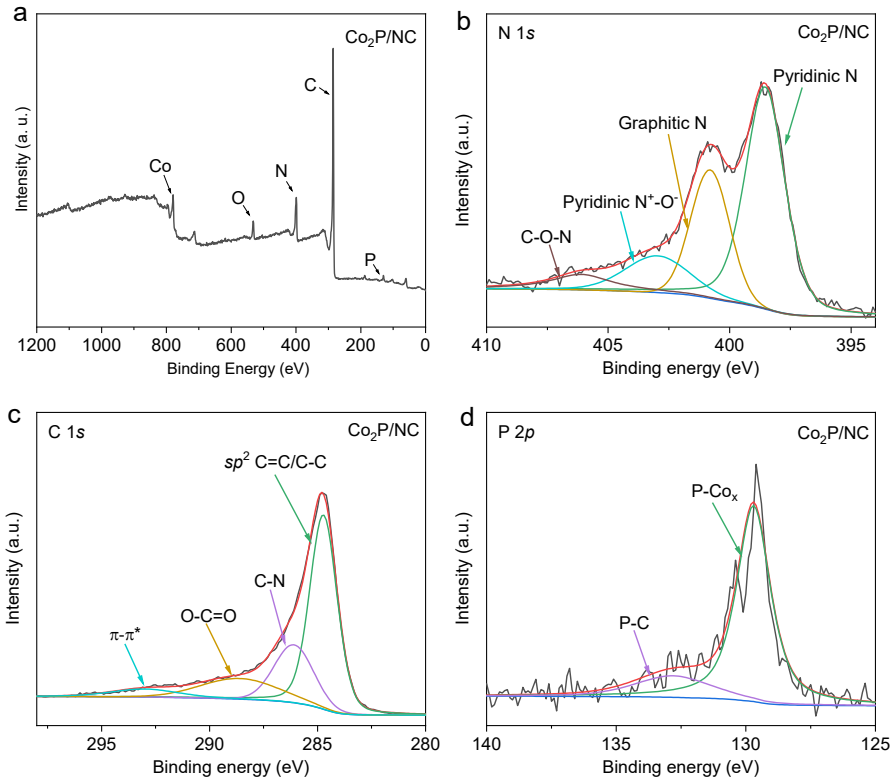
Supplementary Figure 15 | Co *K*-edge EXAFS fitting plots. EXAFS fitting curves of $Co_2P@Co_1$ (a,b), Co_2P/NC (c,d), and Co_2P NP (e,f), catalysts in *k*-space and *R*-space, respectively.



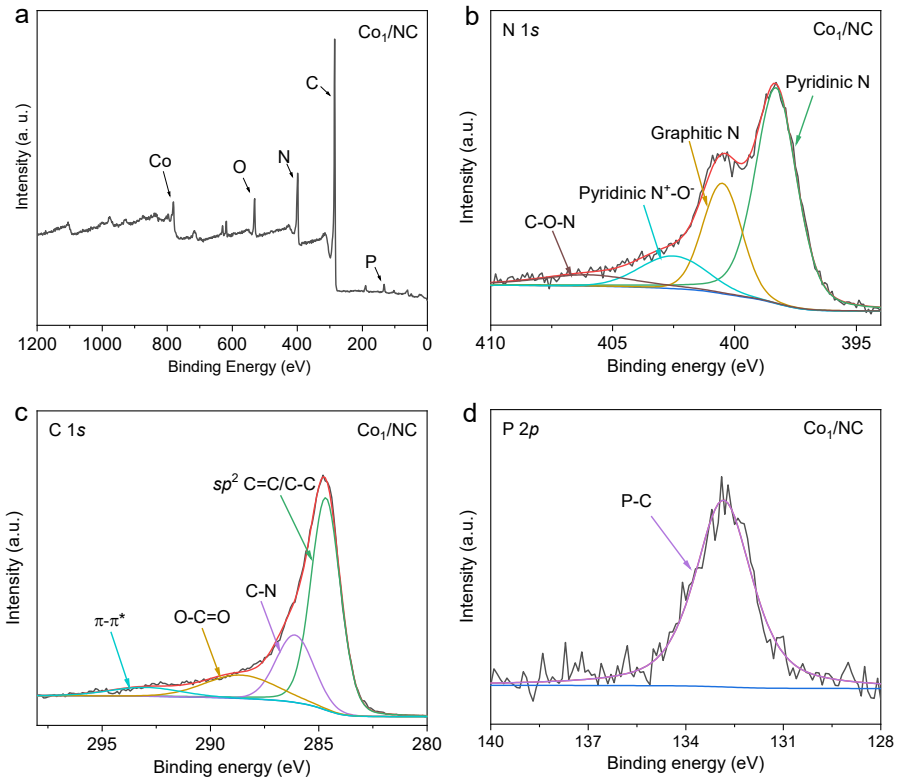
Supplementary Figure 16 | XPS Co 2*p* spectrum of different catalysts[5].



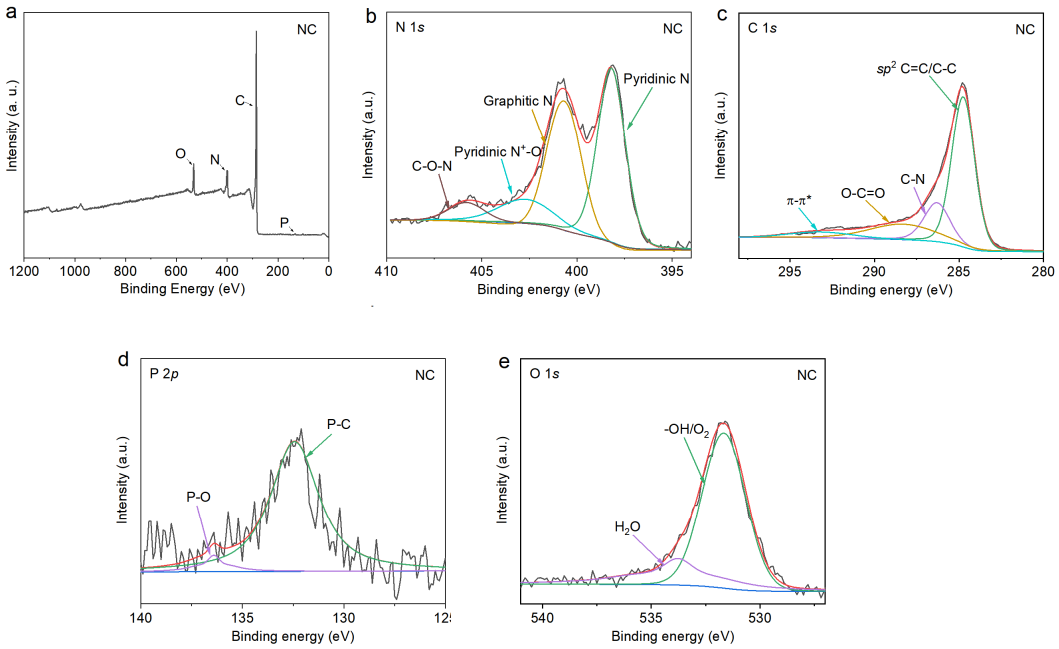
Supplementary Figure 17 | XPS spectra of $Co_2P@Co_1$. The full survey scan (a), N 1*s* (b), C 1*s* (c), P 2*p* (d), and O 1*s* (e).



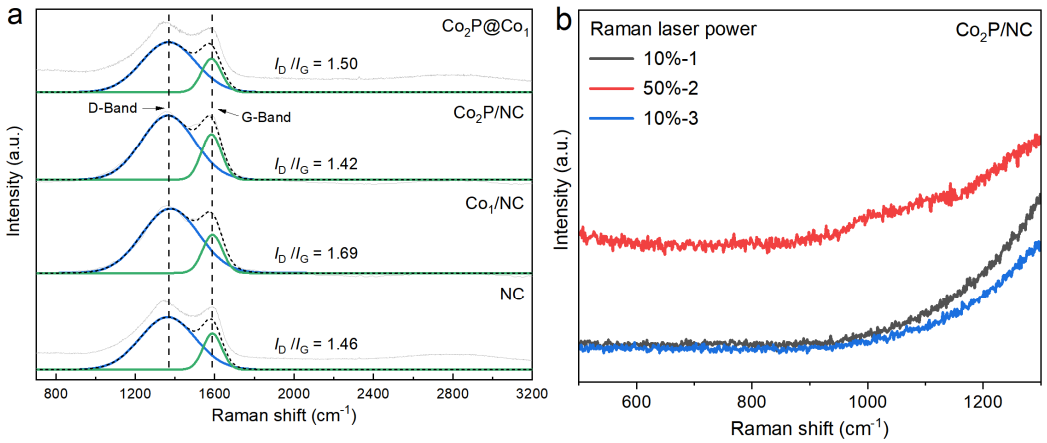
Supplementary Figure 18 | XPS spectra of Co_2P/NC. The full survey scan (a), N 1*s* (b), C 1*s* (c), and P 2*p* (d).



Supplementary Figure 19 | XPS spectra of Co_1/NC. The full survey scan (a), N 1*s* (b), C 1*s* (c), and P 2*p* (d).

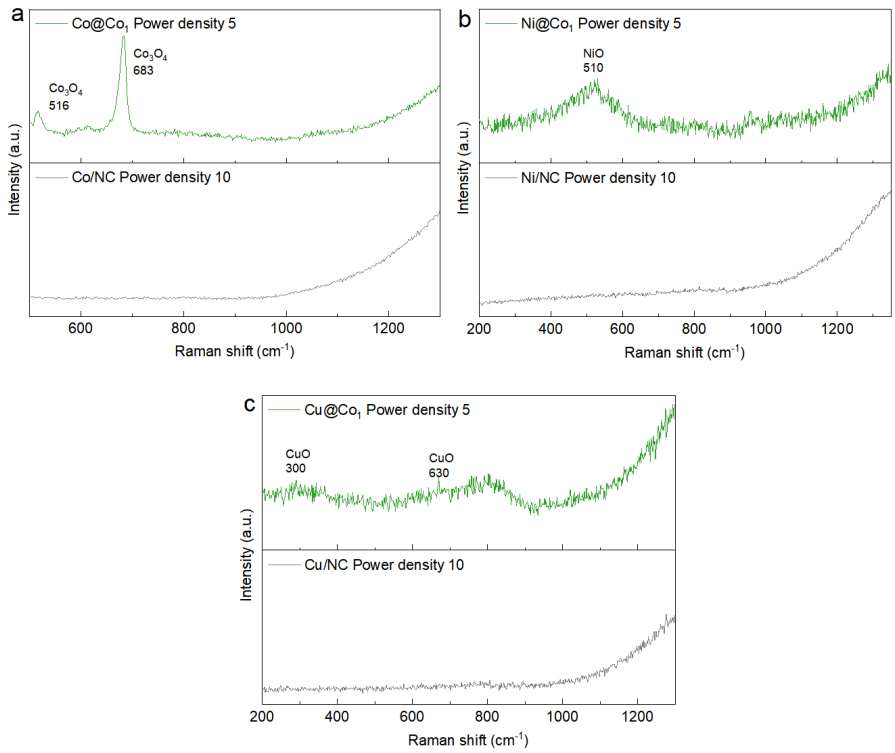


Supplementary Figure 20 | XPS spectra of NC. The full survey scan (a), N 1*s* (b), C 1*s* (c), P 2*p* (d), and O 1*s* (e).

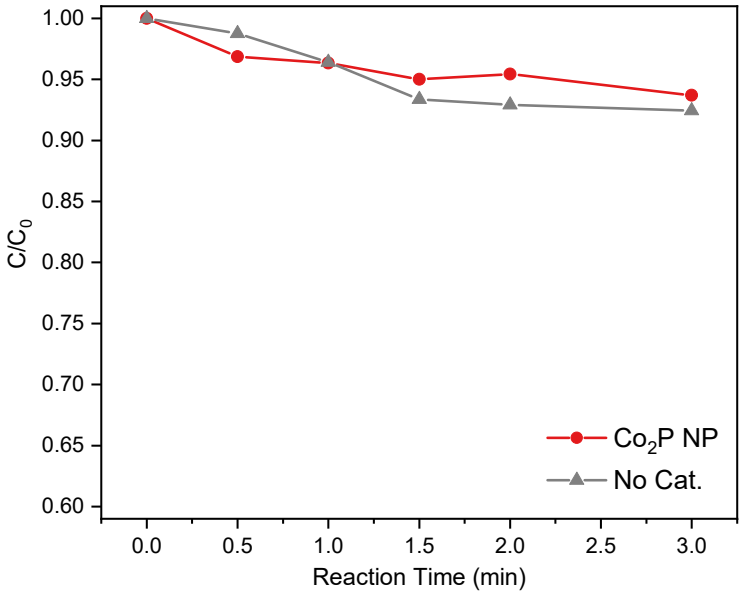


Supplementary Figure 21 | Raman spectra of different catalysts (a), laser induced oxidation experiment of Co_2P/NC (b).

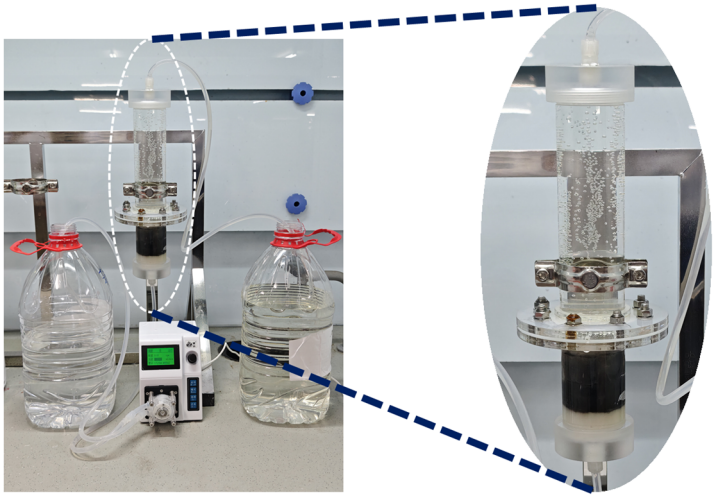
Noted: In (b), for Co_2P/NC, a 10% power laser was initially applied, then increased to 50%, and finally returned to 10%. No peaks were observed.



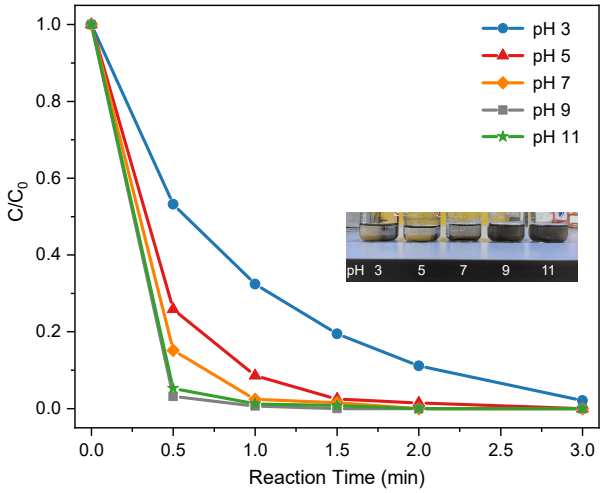
Supplementary Figure 22 | Raman data of $Co@Co_1$ (a) [6], $Ni@Co_1$ (b) [7], and $Cu@Co_1$ (c)[8].



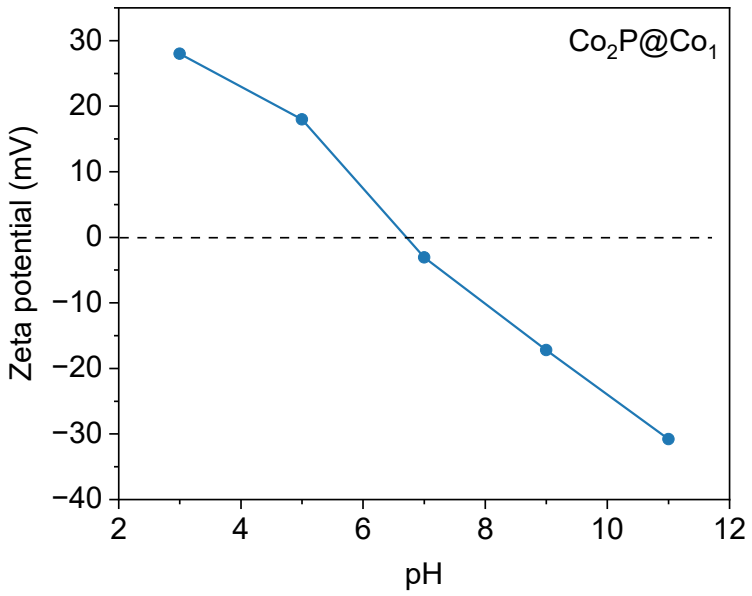
Supplementary Figure 23 | Degradation curves of the pollutant over Co_2P NP and without any catalyst.



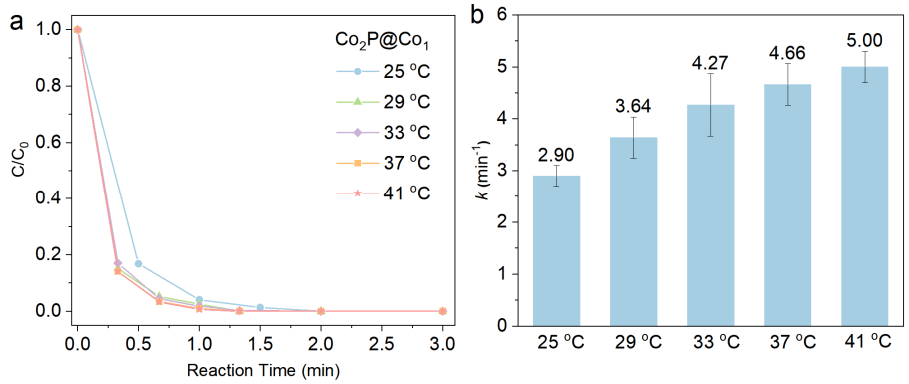
Supplementary Figure 24 | Continuous-flow degradation system. The overall setup is shown on the left, including the reactor, peristaltic pump, and reservoirs. The enlarged view on the right clearly shows the formation of abundant bubbles within the reactor, which are attributed to the activation of PMS by the catalyst, generating oxygen and/or singlet oxygen species, indicating an active reaction process.



Supplementary Figure 25 | Influence of solution pH on PhOH degradation kinetics in $Co_2P@Co_1$ catalytic systems. The reaction rate increases with increasing pH, indicating more efficient catalytic activity under alkaline conditions. This enhancement is likely associated with improved dispersion of the catalyst in solution. The inset shows the visual differences of the reaction systems at various pH values.



Supplementary Figure 26 | Zeta potential of $Co_2P@Co_1$ over different pH.

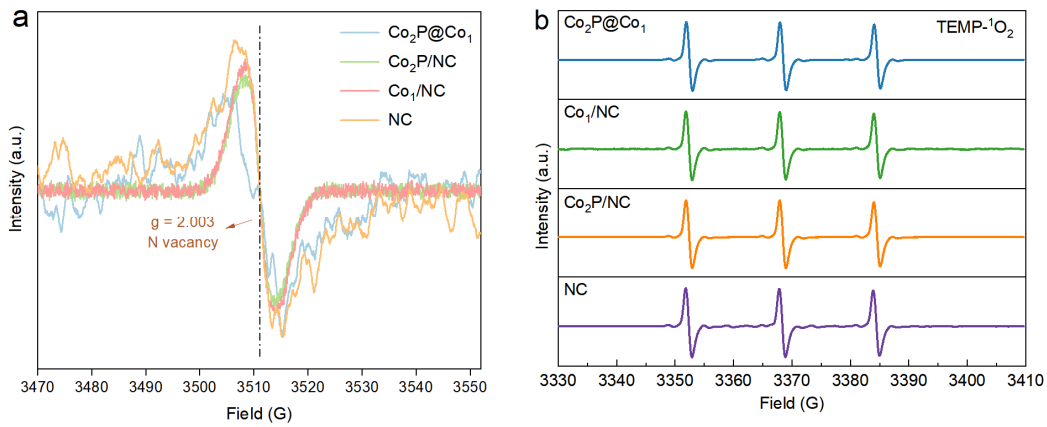


Supplementary Figure 27 | Temperature-dependent degradation kinetics over $Co_2P@Co_1$. Increasing temperature significantly accelerates the reaction rate, as evidenced by the faster decay of C/C_0 (a) and the increased pseudo-first-order rate constants (b), suggesting enhanced catalytic activity and reaction kinetics at elevated temperatures.

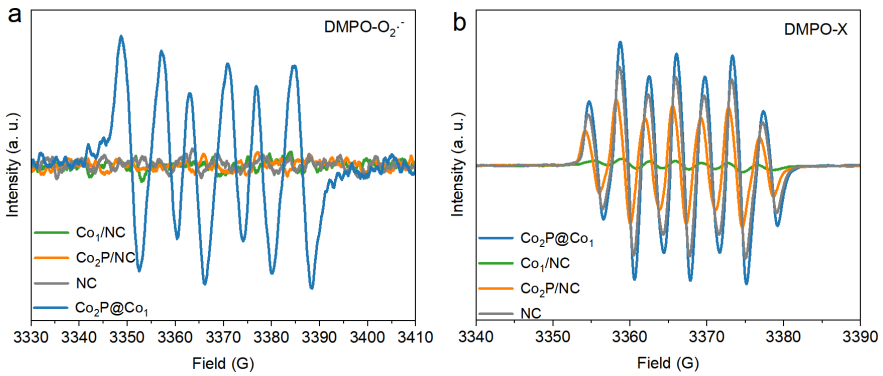


Supplementary Figure 28 | Toxicity assessment of treated water by $Co_2P@Co_1$ based on *E. coli* colonies formation after 12 h cultivation in different water samples: industrial effluents ($\times10^{-2}$) before (a) and after (b) degradation are compared with deionized DI water (c).

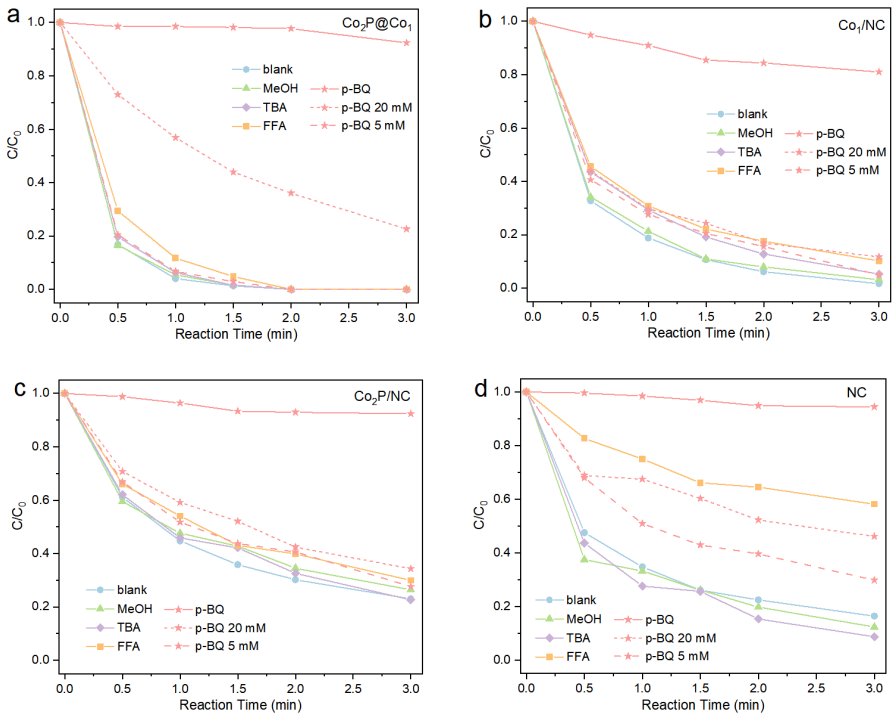
Noted: The industrial wastewater is sourced from BioChem United Pharmaceutical Co.,ltd, Anhui.



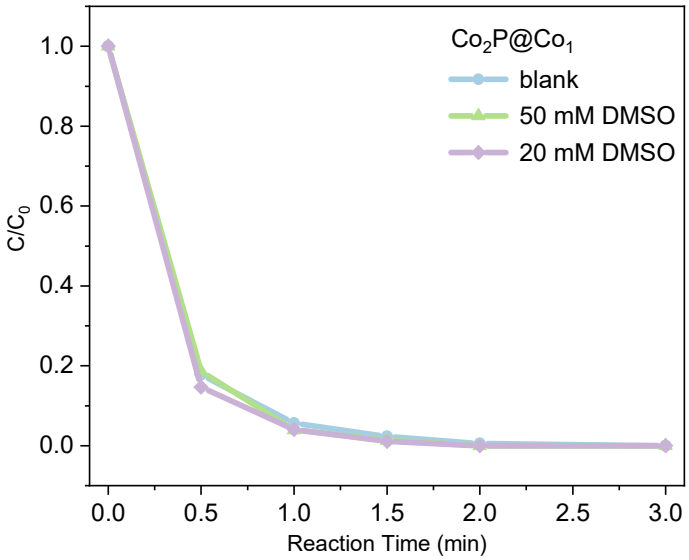
Supplementary Figure 29 | EPR spectra measured at room temperature, solid (a) and $^{1}O_2$ radical detection using TEMP as trapping agents (b).



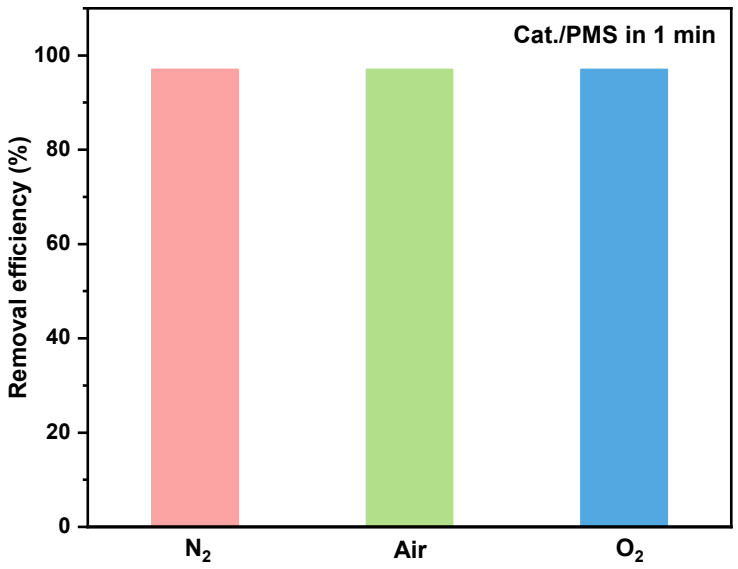
Supplementary Figure 30 | EPR spectra measured at room temperature in methanol (a) and water (b) for superoxide, ·OH and $SO_4^{\cdot-}$ radical detection using DMPO as trapping agents.



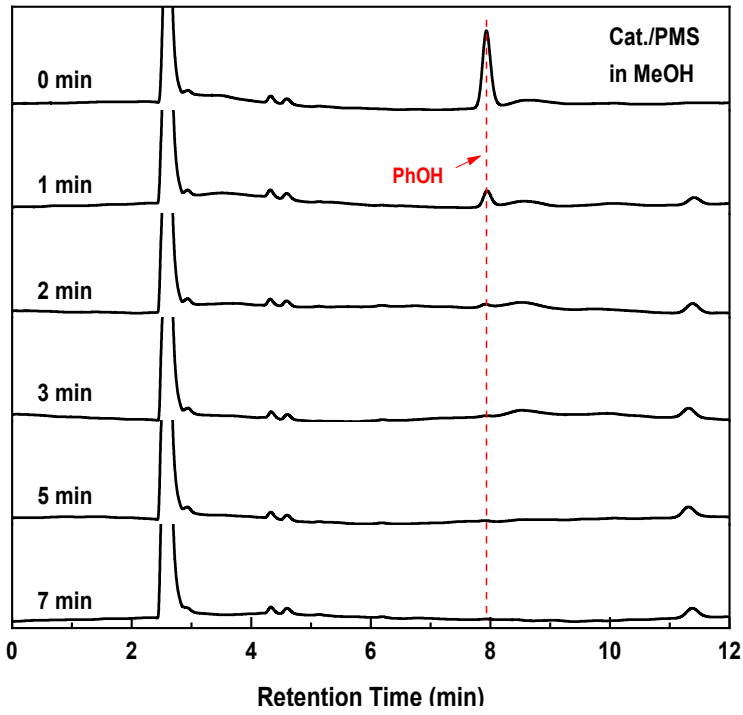
Supplementary Figure 31 | Radical quenching curves of $Co_2P@Co_1$ (a), Co_1/NC (b), Co_2P/NC (c), and NC (d).



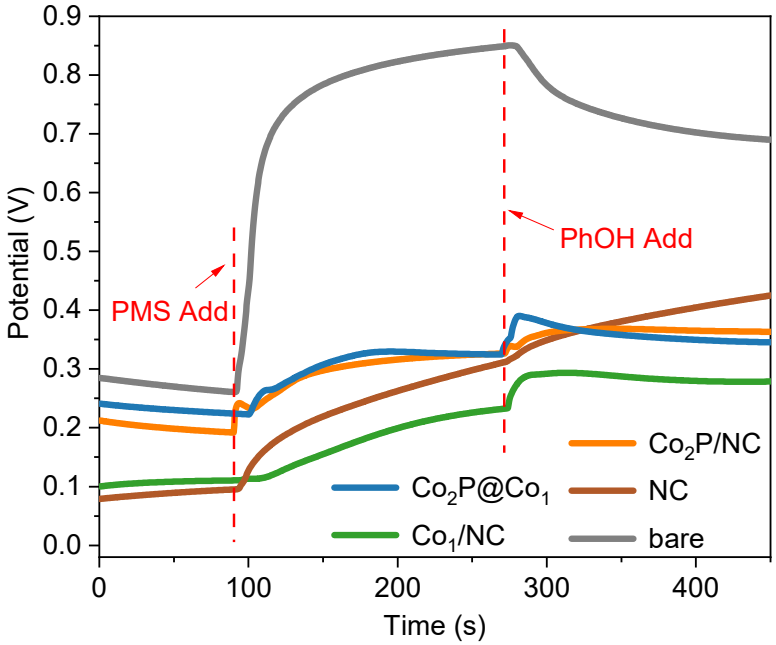
Supplementary Figure 32 | High-valent Co species detection with DMSO.



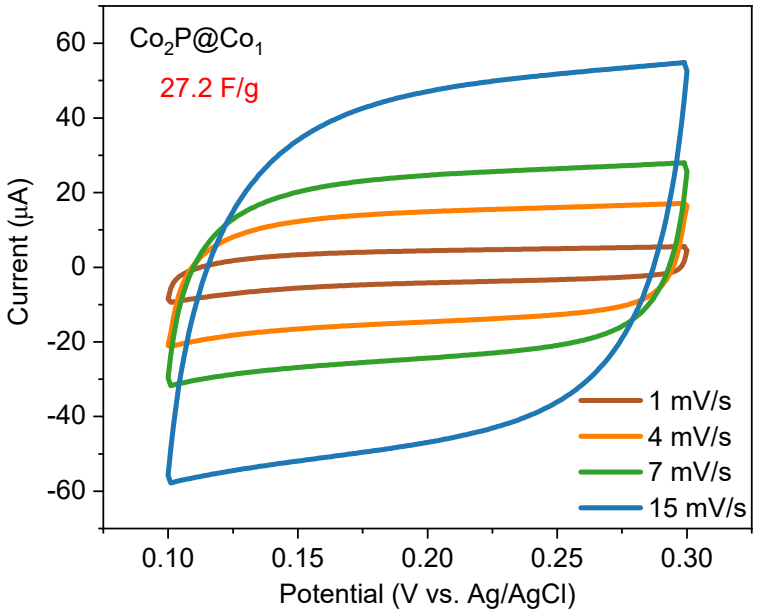
Supplementary Figure 33 | Degradation kinetic of phenol under different atmospheres over $Co_2P@Co_1$ within 1 min.



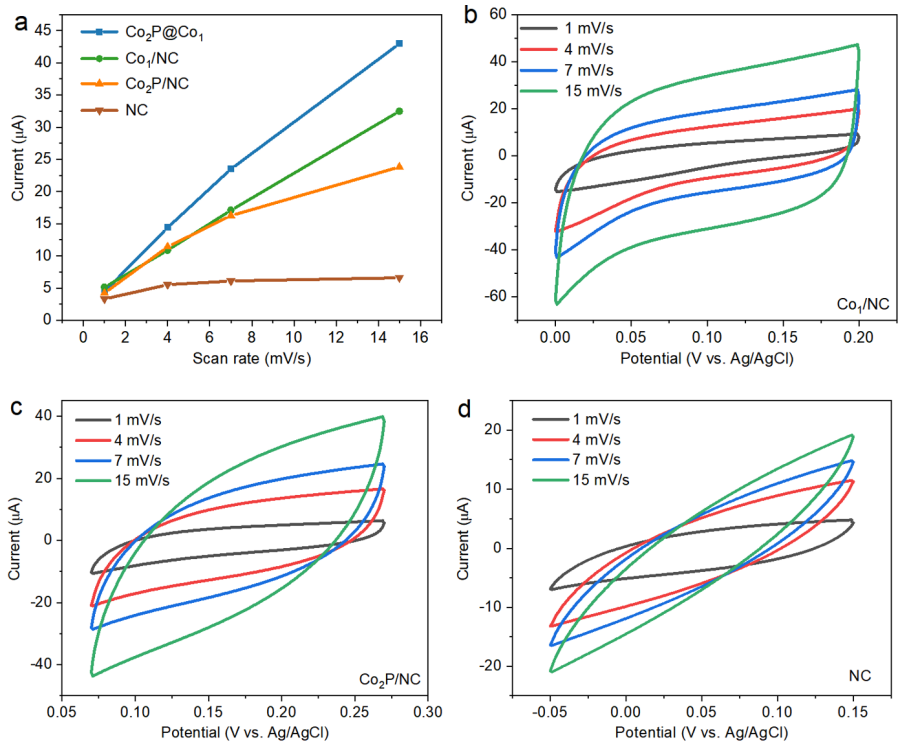
Supplementary Figure 34 | Liquid chromatogram of phenol degradation in methanol over $Co_2P@Co_1$.



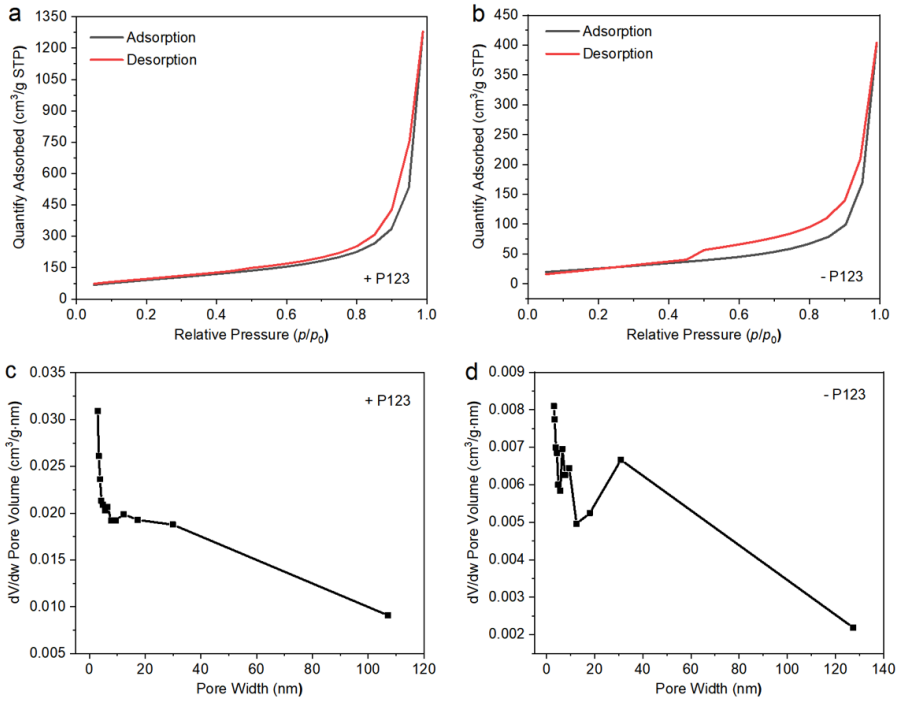
Supplementary Figure 35 | Open-circuit potentials (OCP) changes upon sequential addition of PMS and PhOH.



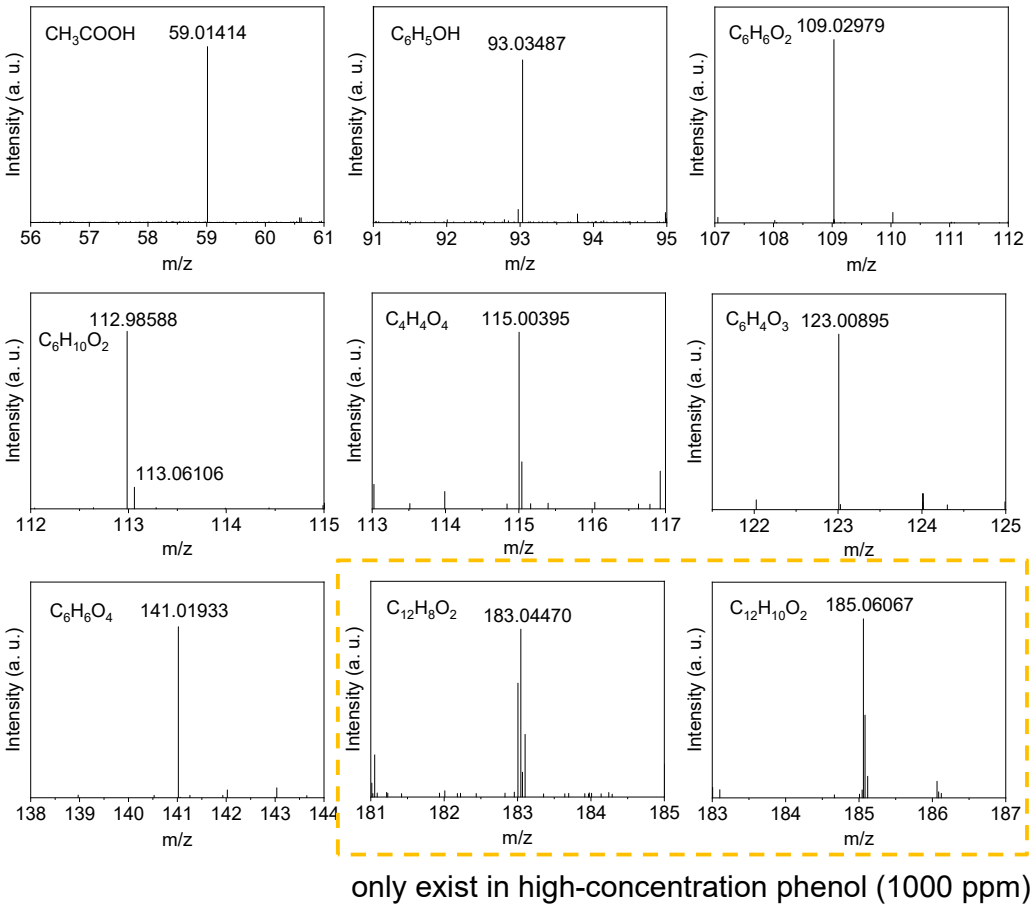
Supplementary Figure 36 | Capacity measurement using CV method of $Co_2P@Co_1$.



Supplementary Figure 37 | Capacitive properties of the samples investigated by CV. (a) Variation of current with scan rate for different catalysts. CV curves of Co_1/NC (b), Co_2P/NC (c), and NC (d). The quasi-rectangular shapes and scan rate-dependent current responses suggest dominant capacitive contributions.

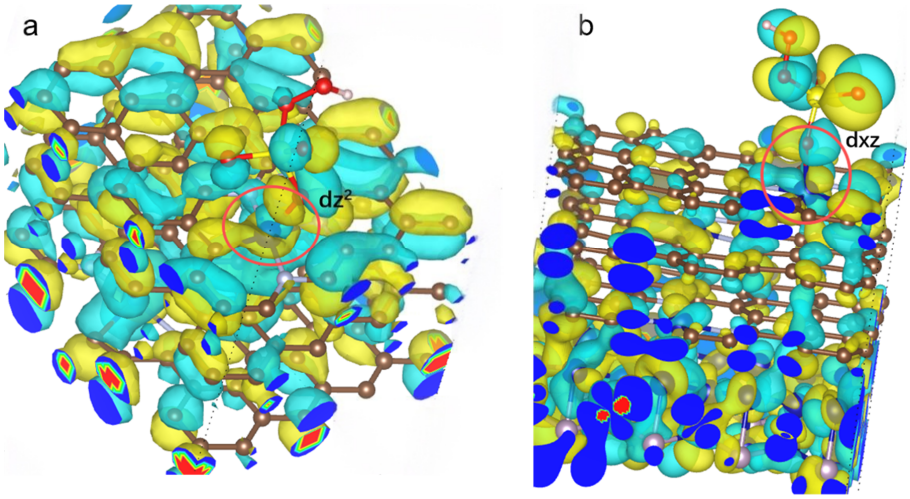


Supplementary Figure 38 | Adsorption isotherms and pore size distributions of catalysts synthesized with (a, c) and without (b, d) the surfactant P123 of $Co_2P@Co_1$.

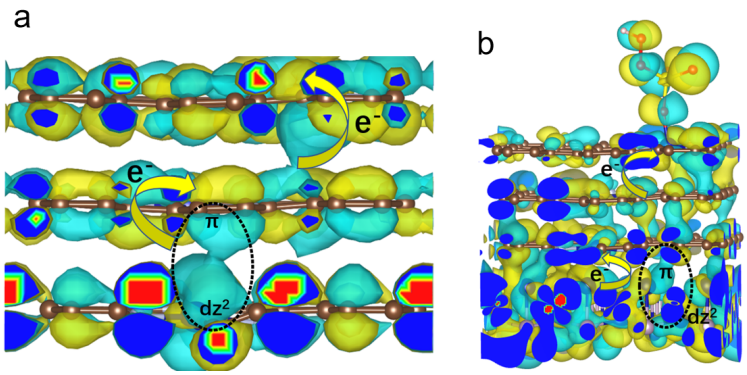


Supplementary Figure 39 | PhOH degradation intermediates detected in $Co_2P@Co_1$ catalytic systems by LC–Orbitrap MS.

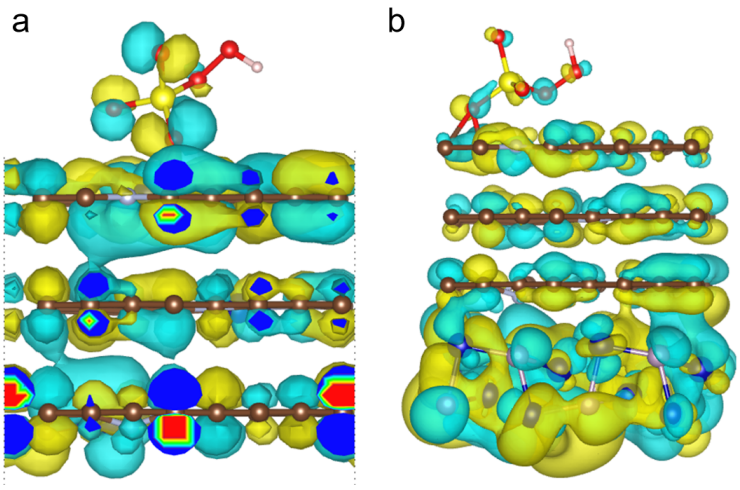
Reaction condition: 200 ppm PhOH, [catalyst] = 0.125 g L^{-1}, [PMS] = 0.98 mM; 1000 ppm PhOH, [catalyst] = 0.15 g L^{-1}, [PMS] = 1.23 mM.



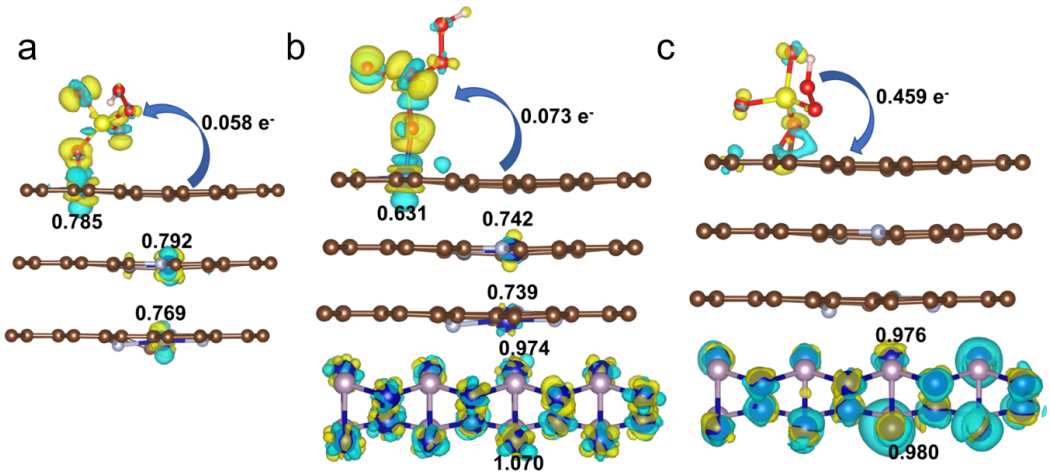
Supplementary Figure 40 | Orbital-resolved isosurfaces illustrating the electronic coupling mechanism with PMS. (a) The d_{z^2}orbital distribution of Co on Co_1/NC. (b) The d_{xz}orbital distribution of Co on Co_2P@Co_1.



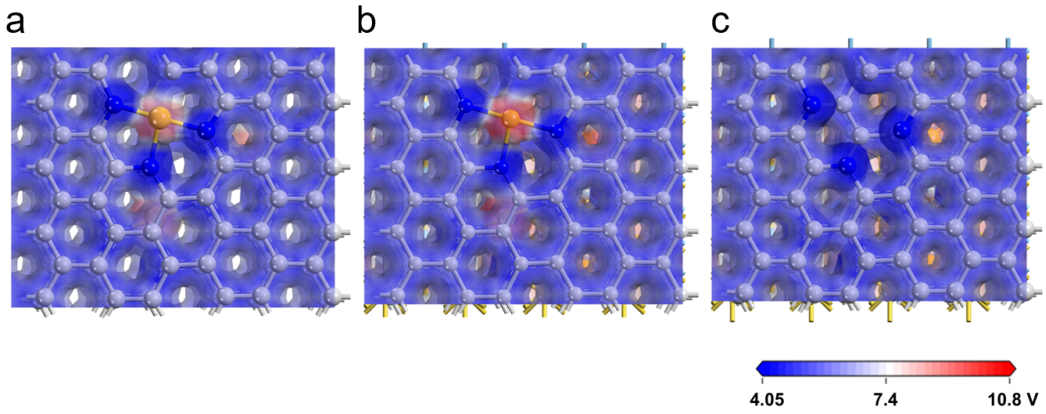
Supplementary Figure 41 | Orbital-resolved isosurfaces illustrating the electronic coupling mechanism in the system. In-plane electron delocalization pathway (e^-) for Co_1/NC (a) and Co_2P@Co_1 (b), revealing the coupling between π orbitals and d_{z^2} states.



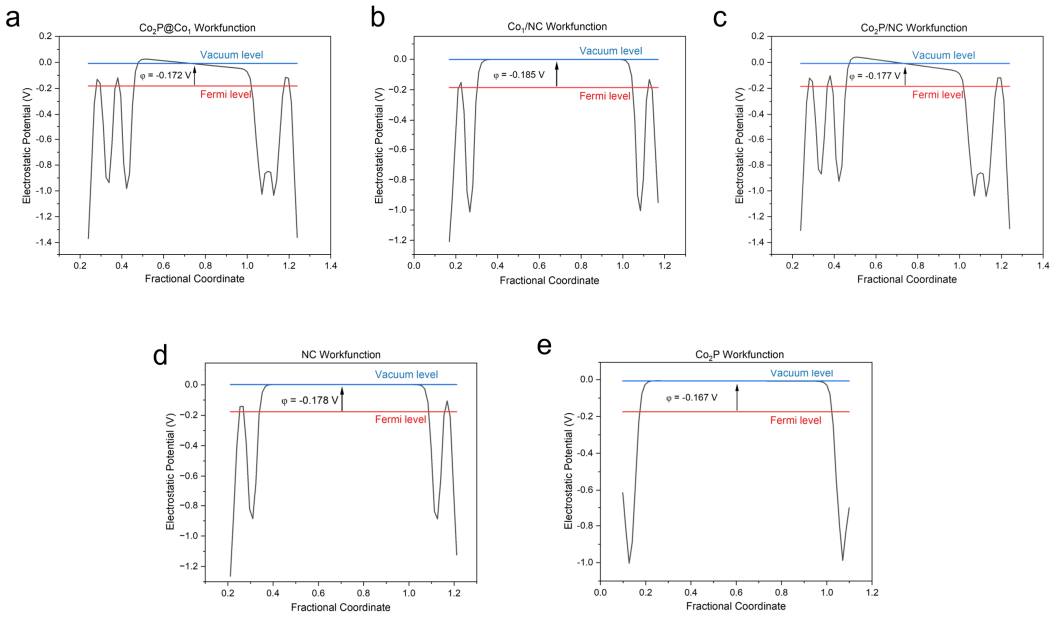
Supplementary Figure 42 | Orbital-resolved isosurfaces illustrating the electronic coupling mechanism for Co_1/NC (a) and Co_2P/NC (b).



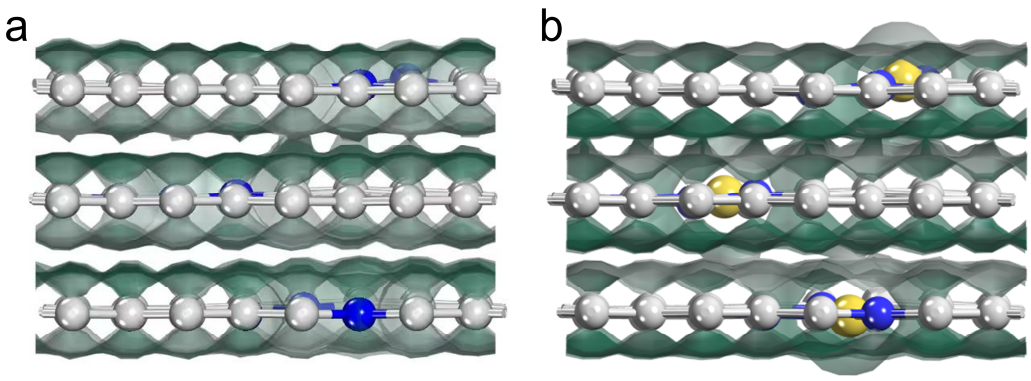
Supplementary Figure 43 | Difference charge density for PMS adsorption on Co_1/NC (a), Co_2P@Co_1 (b) and Co_2P/NC (c).



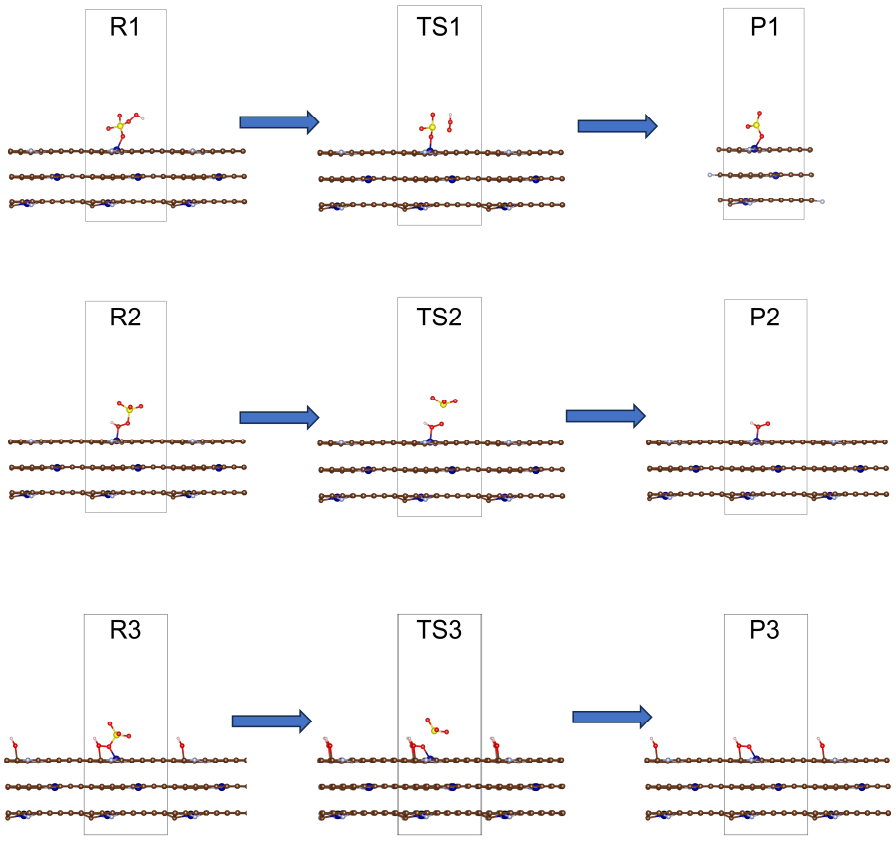
Supplementary Figure 44 | The electrostatic potential distributions for Co_1/NC (a), Co_2P@Co_1 (b) and Co_2P/NC (c).



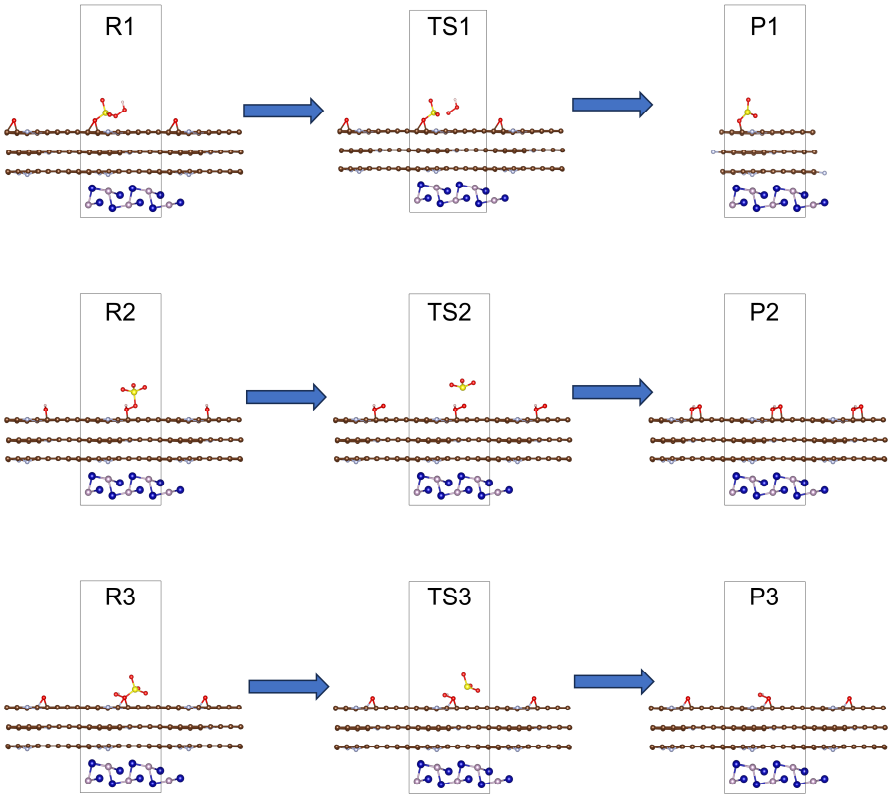
Supplementary Figure 45 | Workfunction of $Co_2P@Co_1$ (a), Co_1/NC (b), Co_2P/NC (c), NC (d) and Co_2P (e).



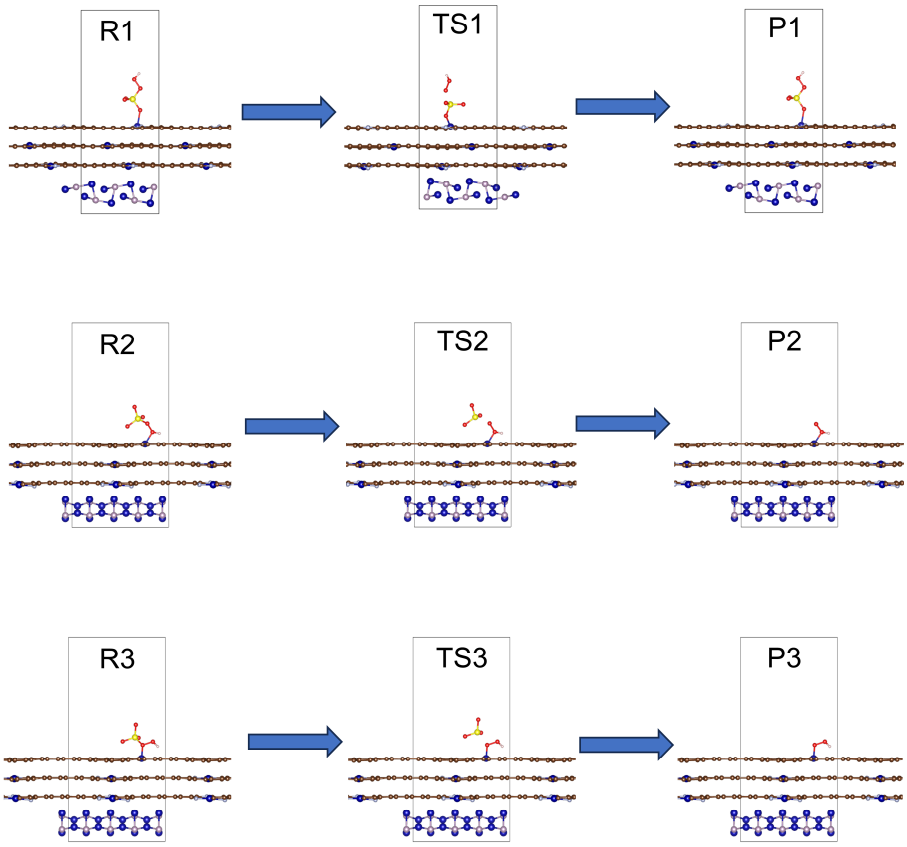
Supplementary Figure 46 | Electron density distribution of (a) NC and (b) Co_1/NC. Isosurface value: 0.13989.



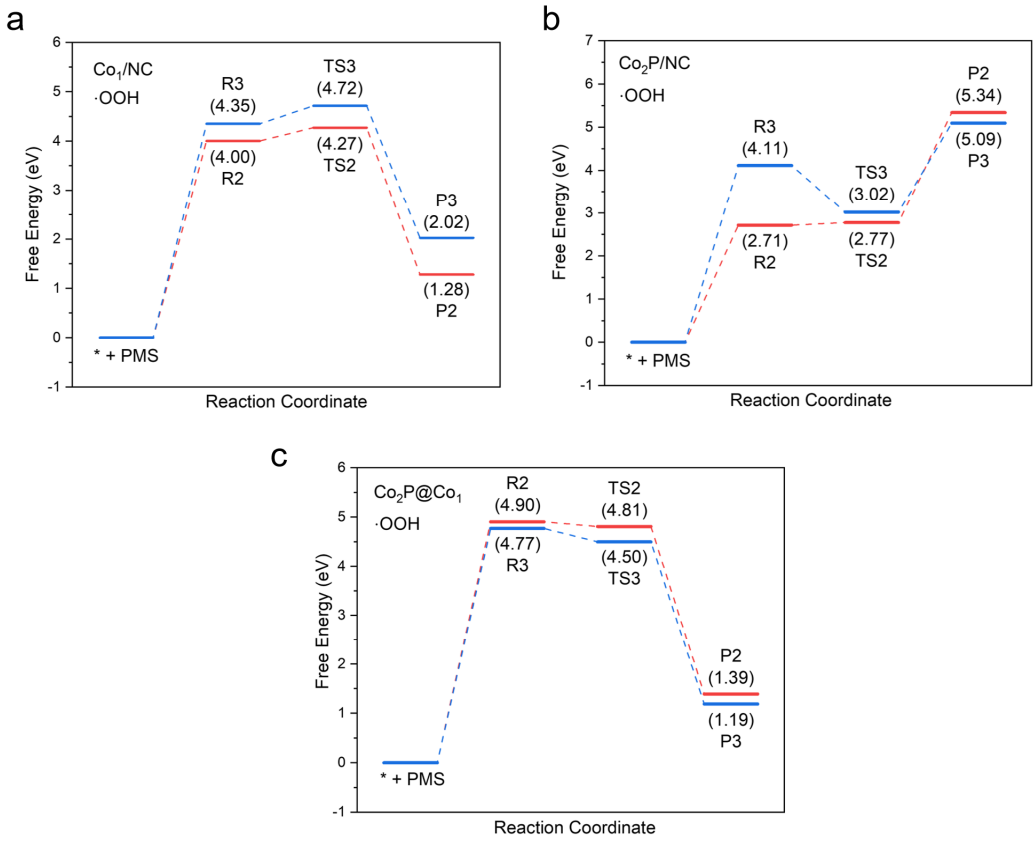
Supplementary Figure 47 | Reaction pathway on Co_1/NC.



Supplementary Figure 48 |Reaction pathway on $Co_2P@Co_1$.



Supplementary Figure 49 | Reaction pathway on Co_2P/NC.



Supplementary Figure 50 | Free energy diagram for PMS activation on Co_1/NC (a), Co_2P/NC (b) and $Co_2P@Co_1$ (c).

Supplementary Table 1. Structural parameters obtained from EXAFS fitting for Co_2P-NP, Co_2P/NC, and Co_2P@Co_1.

Sample	Shell	CN	R(Å)	σ^2 (*10^{-3} Å^2)	ΔE_0 (eV)	R factor
Co_2P NP	Co-P	3.04±0.18	2.16±0.005	11	-1.17	0.010
	Co-Co	2.64±0.18	2.62±0.004	6.5		
Co_2P/NC	Co-N	0.82±0.31	1.97±0.034	3	-9.8	0.010
	Co-P	0.85±0.33	2.27±0.008	6		
	Co-Co	1.92±0.19	2.58±0.005	5		
Co_2P@Co_1	Co-N	1.89±0.14	1.93±0.006	9	0.48	0.004
	Co-P	0.81±0.08	2.23±0.007	7		
	Co-Co	1.82±0.09	2.62±0.004	9		

CN is the coordination number; R is the interatomic distance (the bond length between central atoms and surrounding coordination atoms); σ^2 is the Debye-Waller factor (a measure of thermal and static disorder in absorber-scatterer distances); ΔE_0 is edge-energy shift (the difference between the zero kinetic energy value of the sample and that of the theoretical model). This value of S_0^2 was fixed to be 0.77 as determined from Ni foil. Error bounds that characterize the structural parameters obtained by EXAFS spectroscopy were estimated as CN ± 20%; R ± 1%; σ^2 ± 20%; ΔE_0 ± 20%.

Supplementary Table 2. Fermi level of different catalysts.

	NC	Co_2P	Co_1/NC	Co_2P/NC	$Co_2P@Co_1$
Fermi Energy (eV)	-4.740	-4.628	-5.026	-5.013	-4.929

Supplementary Table 3. Elements analysis of different catalyst. (a. measured by ICP-OES; b. measured by Elemental Analysis (EA)

	Co[a] (wt%)	P[a] (wt%)	C[b] (wt%)	N[b] (wt%)	O[b] (wt%)	C/N[b]
$Co_2P@Co_1$	6.98	1.20	69.87	16.80	5.15	4.16
Co_2P/NC	6.27	1.47	70.86	17.41	3.99	4.07
Co_1/NC	2.03	0.40	78.42	17.14	2.01	4.58
NC	0	0.23	79.61	18.53	1.63	4.30

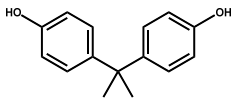
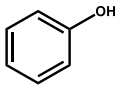
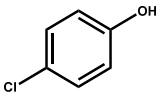
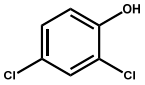
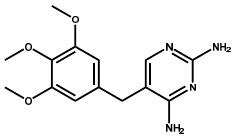
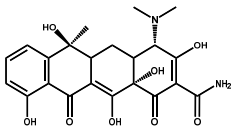
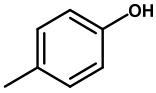
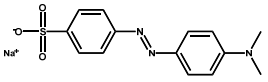
Supplementary Table 4. The solution resistance (R_s) and charge transfer resistance (R_{ct}) from EIS fitting by Z-view.

	R_s (ohm)	R_s error (%)	R_{ct} (ohm)	R_{ct} error (%)
$Co_2P@Co_1$	22.16	5.4698	110.6	0.86976
Co_1/NC	13.8	6.5434	280.7	1.1583
Co_2P/NC	35.69	4.3685	559.1	0.79263
NC	32.19	6.803	482	1.7924

Supplementary Table 5. Textural parameters of samples prepared with (+P123) and without (−P123) surfactant.

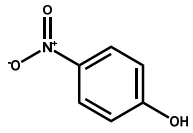
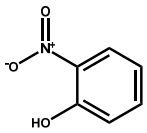
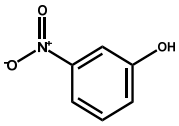
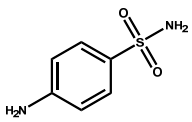
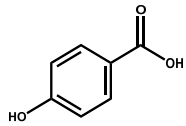
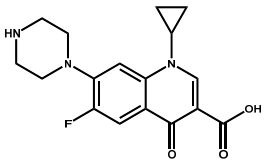
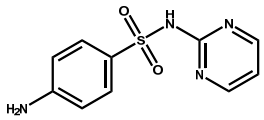
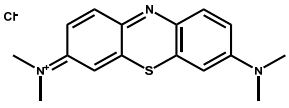
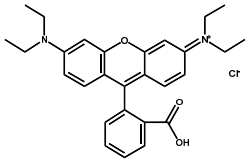
	S_{BET} (m^2 g^{-1})	S_{DFT} (m^2 g^{-1})	Pore Volume (cm^3 g^{-1})	Diameter (nm)
+P123	327.9	262.8	1.937	3.053
-P123	93.7	72.0	0.613	3.06

Supplementary Table 6. Degradation performance of electron-deficient pollutants.

Substance	Formula	k/min^{-1}	LC condition (Methanol : H_2O, λ)
Bisphenol A		2.94	70 : 30, 270 nm
Phenol		2.89	60 : 40, 270 nm
p-Chlorophenol		1.95	70 : 30, 280 nm
2,4-Dichlorophenol		1.76	70 : 30, 280 nm
Trimethoprim		3.53	40 : 60, 240 nm
Tetracycline		3.49	20 : 80 : 1.06, 280 nm CH_3CN: H_2O: HCOOH
p-Cresol		2.54	60 : 40, 270 nm
Methyl orange		2.70	300-600 nm, 463 nm UV-Vis detection

*1.2 mg catalyst, 12 mg PMS, 20 ppm pollutant, 25 °C, air.

Supplementary Table 7. Degradation performance of electron-rich pollutants.

Substance	Formula	k/min^{-1}	LC condition (Methanol : H_2O, λ)
p-Nitrophenol		0.09	70 : 30, 270 nm
o-Nitrophenol		0.18	70 : 30, 270 nm
m-Nitrophenol		0.27	70 : 30, 270 nm
Sulfanilamide		0.54	30 : 70, 270 nm
4-Hydroxybenzoic acid		0.56	60 : 40, 270 nm
Ciprofloxacin		0.72	20 : 80 : 1.06, 280 nm CH_3CN: H_2O: HCOOH
Sulfadiazine		1.01	30 : 70, 280 nm
Methylene blue		1.26	500-750 nm, 664 nm UV-Vis detection
Rhodamine B		3.58	450-650 nm, 550 nm UV-Vis detection

*1.6 mg catalyst, 16 mg PMS, 20 ppm pollutant, 25 °C, air.

Supplementary Table 8. TOC analysis of industrial effluents ($x10^{-2}$) during degradation by Co_2P/Co_1.

TOC	0 min	5 min	10 min	15 min	20 min
1	4.524	1.448	1.394	1.362	1.309
2	4.306	1.443	0.627	0.439	0.268

1. PMS was added only at the beginning;
2. Add the same concentration of PMS every five minutes.

Noted: The reaction conditions were only adjusted by changing the catalyst dosage to 1.5 mg, with all other parameters remaining the same. Samples are collected at 5 min intervals. 2 mL of the reaction solution is directly withdrawn and filtered through a 0.22-μm nylon membrane to quench the reaction. Then, it is diluted to 20 mL for analysis.

Supplementary Table 9. Comparison of degradation performance with previously reported studies.

Catalyst ($g \cdot L^{-1}$)	PMS (mM)	Pollutant ($mg \cdot L^{-1}$)	k_{obs} (min^{-1})	k-value* ($min^{-1} \cdot M^{-1}$)	Mechanism	Ref.
Co_2P@Co_1 (0.03)	0.98	PhOH (20)	2.90	1972.79	Electron-transfer	This work
Co_2P@Co_1 (0.03)	0.98	BPA (20)	2.94	2000.00	Electron-transfer	This work
0.75 wt% Cu-Co_3O_4/Ovs (0.2)	0.3	PhOH (10)	0.26	42.57	Radicals, Electron-transfer	[9]
A/C-$CoMnO_x$ (0.1)	0.16	BPA (10)	1.48	925	Mn^{3+}/Mn^{4+}-Electron-transfer	[10]
$Co_2(V_4O_{12})(bpy)_2$ (0.2)	0.1	BPA (5)	2.795	698.75	$^1O_2$, $SO_4^{\bullet-}$	[11]
S-NCC-5 (0.2)	1.95	PhOH (60)	2.47	380.0	Radicals, $^1O_2$	[12]
Fe-Co-NC (0.1)	0.65	BPA (20)	1.252	385.23	$^1O_2$	[13]
Fe-N-C (0.1)	0.5	BPA (22.8)	0.274	124.94	Fe^{IV}=O, Electron-transfer	[14]
$CoFe_2O_4$/ZnO (0.25)	0.3	PhOH (20)	0.088	23.46	$^1O_2$, $O_2^{\cdot-}$	[15]
0.3Fe-BNC (0.1)	0.2	SMX (10)	1.15	440	$^1O_2$	[16]
$CoMn/CN_{inter}$ DSACs (0.1)	1.0	BPA (9.1)	1.3	118	$^1O_2$	[17]

ZnN_4-Edge (0.05)	3.0	PhOH (94)	0.344	215.57	·OH	[18]
Cu-N_4/C-B (0.1)	0.65	BPA (20)	0.56	172.31	Cu (III)-OH	[19]
2.9% Cu1/NG (0.1)	0.5	BPA (20)	1.18	472	Electron-transfer	[20]
$ZnFeMnO_4$ (0.1)	0.163	BPA (10)	0.43	263.8	Electron-transfer	[21]
Co_1CNCl/S (0.05)	0.4	PhOH (19)	0.952	904.4	Electron-transfer	[22]
CoCN-15 (0.1)	2	BPA (33)	0.239	39.44	Electron-transfer	[23]
CoNC-MSi1 (0.25)	0.4	PhOH (9.4)	1.8	169.2	Electron-transfer	[24]

* The *k*-values were recalculated using the reported parameters and a unified calculation method, instead of directly using the values provided in the literature, to ensure a fair comparison.

Supplementary references:

1. Ha, D.-H. et al. The structural evolution and diffusion during the chemical transformation from cobalt to cobalt phosphide nanoparticles. *J. Mater. Chem.* **21**, 11498 (2011).
2. Carenco, S. et al. Controlled design of size-tunable monodisperse nickel nanoparticles. *Chem. Mater.* **22**, 1340-1349 (2010).
3. Heilmann, M. et al. Advances in nickel nanoparticle synthesis via oleylamine route. *Nanomaterials* **10**, 713 (2020).
4. Wei, Y. et al. Synthesis of stable, low-dispersity copper nanoparticles and nanorods and their antifungal and catalytic properties. *J. Phys. Chem. C* **114**, 15612 (2010).
5. Ren, Y. *et al.* Dual-function surface engineering for enhancing anode stability in alkaline seawater oxidation. *Nat. Commun.* **17**, 5178 (2026).
6. Li, H. et al. Facile synthesis of recyclable Co_3O_4/$Co(OH)_2$/RGO ternary heterostructures with synergistic effect for photocatalysis. *J. Nanopart. Res.* **20**, 279 (2018).
7. Jin, S. et al. Enhanced hydroconversion of lignin-derived oxygen-containing compounds over bulk nickel catalysts though Nb_2O_5 modification. *Catal. Lett.* **147**, 2215 (2017).
8. Akgul, F. A. et al. Physics Influence of thermal annealing on microstructural, morphological, optical properties and surface electronic structure of copper oxide thin films. *Mater. Chem. Phys.* **147**, 987 (2014).
9. Li, Y. H. et al. Unveiling Roles of Nonradical Electron-Donation Pathway in Peroxymonosulfate Activation for Boosted Interfacial Radical Generation. *Angew. Chem. Int. Ed.* e202507772 (2015).
10. Guo, Z.-Y. et al. Crystallinity engineering for overcoming the activity-stability tradeoff of spinel oxide in Fenton-like catalysis. *Proc. Natl. Acad. Sci. U.S.A* **120**, e2220608120 (2013).
11. Lan, M.-Y. et al. Multi-channel electron transfer induced by polyvanadate in metal-organic framework for boosted peroxymonosulfate activation. *Nat. Commun.* **15**, 7208 (2024).
12. Gu, C. H. et al. Ultrafast Water Purification by Template-Free Nanoconfined Catalysts Derived from Municipal Sludge. *Angew. Chem. Int. Ed.* **64**, e202423629 (2025).

13. Li, X. et al. Single Cobalt Atoms Anchored on Porous N-Doped Graphene with Dual Reaction Sites for Efficient Fenton-like Catalysis. *J. Am. Chem. Soc.* **140**, 12469 (2018).
14. Cheng, C. et al. Generation of Fe_{IV}=O and its Contribution to Fenton-Like Reactions on a Single-Atom Iron−N−C Catalyst. *Angew. Chem. Int. Ed.* **62**, e202218510 (2023).
15. Yang, M. et al. Constrained Heterogeneous $CoFe_2O_4$/ZnO/PMS Fenton-Like System for Industrial Wastewater Remediation with Recyclability and Zero Metal Loss. *Angew. Chem. Int. Ed.* **64**, e202421797 (2025).
16. Song, J. et al. Directional Formation of Reactive Oxygen Species Via a Non-Redox Catalysis Strategy That Bypasses Electron Transfer Process. *Adv. Mater.* **36**, 2405832 (2024).
17. Jiang, J. et al. Angstrom Confinement-Triggered Adaptive Spin State Transition of CoMn Dual Single Atoms for Efficient Singlet Oxygen Generation. *Adv. Mater.* **37**, 2417834 (2025).
18. Yu, X. et al. A green edge-hosted zinc single-site heterogeneous catalyst for superior Fenton-like activity. *Proc. Natl. Acad. Sci. U.S.A* **120**, e2221228120 (2023).
19. Zhou, X. et al. Identification of Fenton-like active Cu sites by heteroatom modulation of electronic density. *Proc. Natl. Acad. Sci. U.S.A* **119**, e2119492119 (2022).
20. Wang, B. et al. A Site Distance Effect Induced by Reactant Molecule Matchup in Single-Atom Catalysts for Fenton-Like Reactions. *Angew. Chem. Int. Ed.* **61**, e202207268 (2022).
21. Guo, Z.-Y. et al. Electron delocalization triggers nonradical Fenton-like catalysis over spinel oxides. *Proc. Natl. Acad. Sci. U.S.A* **119**, e2201607119 (2022).
22. Zhu, Z.-S. et al. Multidimensional engineering of single-atom cobalt catalysts for ultrafast Fenton-like reactions. *Nat. Water* **3**, 211 (2025).
23. Zhu, Z. S. et al. Atomic-Level Engineered Cobalt Catalysts for Fenton-Like Reactions: Synergy of Single Atom Metal Sites and Nonmetal-Bonded Functionalities. *Adv. Mater.* **36**, 2401454 (2024).
24. Meng, Y. et al. Nanoconfinement steers nonradical pathway transition in single atom fenton-like catalysis for improving oxidant utilization. *Nat. Commun.* ***15***, 5314 (2024).